Monthly Notices of the ROYAL ASTRONOMICAL SOCIETY
MNRAS **482,** 588–605 (2019)
Advance Access publication 2018 October 8
doi:10.1093/mnras/sty2716

Numerical study of the cascading energy conversion of the reconnection current sheet in solar eruptions

Jing Ye,[1,2,3]★ Chengcai Shen,[4] John C. Raymond,[4] Jun Lin[1,2]★ and Udo Ziegler[5]

[1]*Yunnan Observatories, Chinese Academy of Sciences, PO Box 110, Kunming, Yunnan 650216, China*
[2]*Center for Astronomical Mega-Science, Chinese Academy of Sciences, Beijing 100012, China*
[3]*Key Laboratory of Modern Astronomy and Astrophysical, the Ministry of Education, Nanjing University, Nanjing, 210000, China*
[4]*Smithsonian Astrophysical Observatory, 60 Garden Street, MS 15, Cambridge, MA 02138, US*
[5]*Astrophysikalisches Institut Potsdam, D-14482 Potsdam, Germany*

Accepted 2018 October 2. Received 2018 September 9; in original form 2018 June 30

ABSTRACT

Magnetic reconnection plays an important role in the energy conversion during solar eruptions. In this work, we present a resistive magnetohydrodynamical study (2.5D) of a flux rope eruption based on the Lin and Forbes model regarding cascading reconnection. We use a second-order Godunov scheme code, to better understand the physical mechanisms responsible for high reconnection rates and the internal structure, particularly in chaotic or turbulent regions, of the coronal mass ejection (CME)/flare current sheet (CS). Two sets of simulations with Lundquist numbers of 1.18×10^5 and 2.35×10^5 in the vicinity of the CS, generating a slow CME and a moderate one, show global dynamic features largely consistent with the flare model. Looking into the fine structure of the CS, magnetic reconnection employs simultaneously the Sweet–Parker mode and time-dependent small-scale Petschek patterns in the early stage. As the flux rope rises, the outflow region becomes turbulent, which further enhances the reconnection rates. Our results show that coalescence and fusion processes of plasmoids provide a large number of small, transient local diffusion regions to dissipate magnetic energy, and confirm that the dissipation starts at macro-MHD scales rather than ion inertial lengths. The two runs have the same range of the local reconnection rates (10^{-4}–0.3) relevant to CMEs. The fast rates are closely proportional to the square of the aspect ratio of multiple small-scale CSs. The topology of the magnetic field and the turbulence spectrum of the energy cascade are statistically addressed as well.

Key words: magnetic reconnection – MHD – turbulence – Sun: coronal mass ejections (CMEs).

1 INTRODUCTION

In the process of solar eruptions, a long current sheet (CS) generally forms connecting the flare and coronal mass ejection (CME). Magnetic reconnection modifies the magnetic topology and plays a key role in the energy dissipation. It converts magnetic energy into plasma kinetic and thermal energy, and accelerates particles. When stretched or squeezed, the neutral region including an X-type point collapses to a CS of complex structures (Priest & Forbes 2000). Several pieces of evidence indicate the presence of long reconnecting CME/flare CSs, which are thought to be crucial in the triggering and development of CMEs. Since the high temperature emission line of [Fe XVIII] inside CME/flare CSs was reported by Ciaravella et al. (2002), the high temperature emission of CS has been widely explored. Innes, McKenzie & Wang (2003) studied the 2002 April 31 event and reported emission of the high temperature spectral line [Fe XXI] observed by SOHO/SUMER. For this event, Raymond et al. (2003) pointed out that the [Fe XVIII] line observed behind the front of the fast CME was likely the post-CME CS. The high temperature lines also were studied by Bemporad et al. (2006), Ciaravella & Raymond (2008), and Liu et al. (2010). Recently, Li et al. (2018) and Warren et al. (2018) reported [Fe XXIV] emission from the reconnection CS in the 2017 September 10 eruption, and investigated its internal dynamical fine structure.

Many studies suggest that the reconnecting CS also can be detected in white light observations. Webb, Burkepile & Forbes (2003) reported that a bright ray appears in the wake of the CME and lasts for hours or days in half of CMEs observed by LASCO (St. Cyr, Plunkett & Michels 2000). Ko et al. (2003) and Lin et al. (2005) made detailed studies of LASCO and UVCS observations

★ E-mail: yj@ynao.ac.cn (JY); jlin@ynao.ac.cn (JL)

and suggested that the bright band above the cusp structure indicates the reconnection CS. And Ray-like features behind CMEs are found to be related to a post-CME CS by Patsourakos & Vourlidas (2010) from multiviewpoint coronagraph observations. EUV images of reconnecting CSs are seen in Solar Dynamics Observatory/Atmospheric Imaging Assembly (SDO/AIA) observations. For example, Reeves & Golub (2011) reported a likely CS above a C4.9 flare observed on 2010 November 3, in which the hot plasma has been seen. For the same case, the inflow-outflow events in CSs have also been seen with AIA by Savage et al. (2012).

Different magnetic configurations are considered for solar eruption mechanisms. The famous Kopp–Pneuman model (Kopp & Pneuman 1976) for the two-ribbon flare suggests that the eruption jets form a fully open magnetic field enclosing a neutral CS. The open field releases the energy stored in the force-free arcade via magnetic reconnection in the CS and then relaxes into a closed structure. Lin & Forbes (2000) describe a catastrophe model that gives an analytical solution for the equilibrium curve for the CME eruption. When the pre-existing flux rope reaches the critical point, it erupts. This model predicts the formation of a large-scale CS between the flare and the CME and points out that magnetic reconnection plays an essential role for the successful eruption. Alternative models for triggering eruptions are available, such as the sheared arcade model (Mikić & Linker 1994; Reeves et al. 2010), the breakout model (Antiochos, DeVore & Klimchuk 1999; Karpen, S.K. & DeVore 2012), and the kink and torus instability models (Titov & Démoulin 1999; Török & Kliem 2005), which are not discussed here.

A great deal of theoretical and numerical work based on the 2D catastrophe model of Lin & Forbes (2000) has been done. Wang, Shen & Lin (2009) and Wang et al. (2015) studied numerically the wave-like phenomena and the formation of EUV waves in solar eruptions. On the other hand, Mei & Lin (2008) reported numerical experiments on the equilibrium curves associated with different kinds of sources underneath the photosphere for triggering the eruptions. Recently, Mei et al. (2017) performed solar eruption simulations driven by the T&D model (Titov & Démoulin 1999) to study magnetic reconnection in three dimensions. Their results suggest that the sectional view of the global magnetic structure as well as the fine structure of the CS in the (x, z) plane shows an analogous configuration with the previous 2D simulations.

How the internal structure of CS could be responsible for the energy conversion efficiency is still debated. To allow the eruption to continue, the reconnection process generally needs to occur at a reasonably fast rate. In MHD theory, the process of energy conversion is divided into two steps: ideal MHD regime and non-ideal MHD regime. The ideal MHD regime covers the scales of the energy transfer without dissipation, while non-ideal effects introduce a resistivity or magnetic diffusion in the MHD model. Cowling (1953) points out that, if the ohmic dissipation is the only reason for flares, the CSs with the thickness of several metres provide efficient means to dissipate the energy necessary for flare eruption. However, in the Sweet-Parker model conservation of mass limits the length of the CS to roughly its thickness divided by the inflow Alfvén Mach number, which gives a reconnection rate too slow to account the rapid energy release observed. Subsequently, Petschek (1964) found that, as the MHD instabilities start developing, the aspect ratio of the CS reaches an instability threshold which results in fast energy release by magnetic reconnection and the generation of slow mode shocks in outflow regions. The tearing mode is one of the most important mechanisms responsible for breaking the CS into small-scale magnetic islands or plasmoids (Furth, Killeen & Rosenbluth 1963). Together with the plasmoid instability (Loureiro, Schekochihin & Cowley 2007), externally generated turbulence (Lazarian & Vishniac 1999) or internally generated turbulence (Servidio et al. 2010), these different dissipation styles may even work simultaneously to yield a much more complex pattern and more efficient diffusion that dominated only by a single mechanism (Mei et al. 2012).

Recent work with flare simulations shows that even as the energy cascades from large-scale structure into small-scale patterns, the blobs undergo coalescence and fusion processes to form large plasmoids again (Bárta et al. 2011; Shen et al. 2013; Ni et al. 2015). Those simulations suggest that the further energy dissipation takes place in local diffusive regions via cascading reconnection. At the later stages of the reconnection process, a dynamic balance of the evolution and reconnection rate eventually tends to be constant independent of the initial configuration (Loureiro et al. 2007; Shen et al. 2013). Thanks to the rapid computing ability development in the last decade, the cascading process can be observed at high resolution in numerical experiments. The cascading reconnection outer scale is found to be at least one order of magnitude smaller than the global scale and significant dissipation at macroscale is found in many works. The index of the power spectrum parallel to the local magnetic field is $k_{||} = 2.14$ compared to the perpendicular one $k_{\perp} = 5/3$, which reveals the anisotropy of the turbulence in CSs. Recently, the analytical work of Forbes, Seaton & Reeves (2018) also demonstrates that, to achieve fast reconnection, MHD turbulence could be an important candidate to shorten the length of the diffusion region.

In this study, we investigate the eruption of a pre-existing flux rope driven by a quadrupole source buried below the photosphere, including gravitational stratification, resistivity, and viscosity. A realistic plasma environment is considered along the direction perpendicular to the surface of the Sun. Lin (2002) compared the dynamical properties of CMEs in different plasma environments. His work suggested that the S&G model (Sittler & Guhathakurta 1999) allows for a more reasonable correlation between CMEs and flare properties as well as a better estimation of the reconnection speed compared to an isothermal atmosphere. The adaptive mesh refinement (AMR) technique is utilized inside the CS to reduce the numerical dissipation and capture the plasmoid behaviour in the global magnetic disruption background. We analyse exhaustively both the global energy conversion and the energy flow around the CS as well as the magnetic energy spectrum inside. Plasmoid coalescence via magnetic reconnection and the local current geometry are also studied for CMEs of different velocities.

The paper is organized as follows. In Section 2, we present the resistive 2.5D MHD equations including the physical processes incorporated in this work. The initial magnetic field is computed from three sources: the quadrupole source, the flux rope and its mirror image, and the boundary conditions are specified for the particular cases. We also compute the numerical diffusion inside the CS over a period of time to make sure that the accumulated errors would not introduce significant false currents via numerical reconnection. The numerical results are categorized by global evolution and local topology given in Section 3. Lastly, the conclusions and the discussion are presented in Section 4.

2 NUMERICAL MODEL DESCRIPTION

The MHD simulation investigated here is analytically formalized by Forbes, Priest & Isenberg (1994). The evolution of the system can be adequately described by a 2.5D magnetic disruption MHD model including gravity, viscosity, and resistivity in Cartesian geometry:

$$\partial_t \rho + \nabla \cdot (\rho \boldsymbol{v}) = 0 \tag{1}$$

$$\partial_t e + \nabla \cdot \left[(e + p + \frac{1}{2\mu}|\boldsymbol{B}|^2)\boldsymbol{v} - \frac{1}{\mu}(\boldsymbol{v} \cdot \boldsymbol{B})\boldsymbol{B} \right] = \rho \boldsymbol{g} \cdot \boldsymbol{v} + \nabla \cdot \left[\boldsymbol{v}\tau + \frac{\eta}{\mu}\boldsymbol{B} \times (\nabla \times \boldsymbol{B}) \right] \tag{2}$$

$$\partial_t(\rho \boldsymbol{v}) + \nabla \cdot \left[\rho \boldsymbol{v}\boldsymbol{v} + (p + \frac{1}{2\mu}|\boldsymbol{B}|^2)\boldsymbol{I} - \frac{1}{\mu}\boldsymbol{B}\boldsymbol{B} \right] = \nabla \cdot \tau + \rho \boldsymbol{g} \tag{3}$$

$$\partial_t \boldsymbol{B} = \nabla \times (\boldsymbol{v} \times \boldsymbol{B} - \eta \nabla \times \boldsymbol{B}) \tag{4}$$

where $e = p/(\gamma - 1) + 1/2\rho v^2 + \boldsymbol{B}^2/2\mu$ is the total plasma energy per unit volume (including thermal energy, kinetic energy, and magnetic energy), η is the resistivity, μ is the magnetic permeability in vacuum, $\tau = \nu[\nabla \boldsymbol{v} + (\nabla \boldsymbol{v})^T - 2(\nabla \cdot \boldsymbol{v})\boldsymbol{I}/3]$ is the stress tensor, ν is the dynamic viscosity coefficient, $\rho \boldsymbol{g}$ is the gravity force, and $\gamma = 5/3$ the ratio of specific heats. To complete the above equations, the divergence-free condition ($\nabla \cdot \boldsymbol{B} = 0$) should be satisfied at all times of the evolution.

In the framework of the catastrophe mechanism for the solar eruption, the loss of the equilibrium is purely mechanical, or ideal-MHD, in which diffusion or dissipation of the magnetic field does not occur. This happens when the coronal magnetic configuration evolves gradually through a sequence of equilibrium states to certain critical states at which any further evolution in the system turns dynamic. At a critical state, the system tends to jump, within the Alfven time-scale, from one equilibrium state to another one at a lower energy, and this jump constitutes the 'catastrophe'.

Since the energy driving the eruption comes from the photosphere as a result of deformation of the coronal magnetic field, of which the footpoints are anchored in the photosphere and move unceasingly with the photospheric plasma, any attempt to explain the storage of the energy in the coronal magnetic field must consider the photosphere as a reservoir of the energy, namely variations of the coronal magnetic field during the gradually evolutionary phase. Usually, forms of the change in the photosphere include the plasma motion, decay or enhancement of the photospheric magnetic field as a result of submerging or emerging of the magnetic structure, magnetic reconnection (cancellation), and so on. Analytic studies, numerical experiments, and observations have confirmed that all these causes, except the enhancement of the photospheric magnetic field, could play the role in triggering the eruption (Ding, Hong & Wang 1987; Feynman & Martin 1995; Antiochos et al. 1999; Chen & Shibata 2000; Forbes 2000; Amari et al. 2003; Lynch et al. 2005; Forbes et al. 2006; Jiang et al. 2012; Yan et al. 2012; Schmieder, Démoulin & Aulanier 2013).

For the eruption discussed in this work, the catastrophic loss of equilibrium in the coronal magnetic configuration results from the decay of the magnetic field in the photosphere, which has been confirmed reasonable by the analytic investigation of Isenberg, Forbes & Demoulin (1993), has recently further confirmed numerically by Xie et al. (2017). They noticed that the system evolves roughly following the way given by the analytic solution, and a critical state does exist, at which the loss of equilibrium in the system eventually took place as a perturbation was imposed. Their results definitely indicate that the loss of equilibrium in the system in the catastrophic fashion does occur as the system eventually evolves to the critical state driven by the decay of the photospheric magnetic field. In this work, we further look into the dynamic behaviour of the system after the loss of equilibrium. The initial state of the system is selected slightly deviating from the critical one to push the system to evolve faster so that we are able to more focus on the topic of our interests.

This work is performed using the AMR embedded code NIRVANA3.8 (Ziegler 2004, 2005, 2008, 2011), which applies the block clustering parallel infrastructure (Hilbert space-filling curve mapping) to manage the data communication. The NIRVANA code employs the second-order Godunov scheme using the finite volumes method, and the integral system then turns into many local Riemann problems solved by HLL-type (Harten–Lax–van Leer) solvers. The divergence-free condition of the magnetic field can be guaranteed by the constrained transport method and the conserved parameters will be updated explicitly in time by the Runge–Kutta calculator (RK3, RK4). We stress that the addition of Spitzer thermal conduction leads to an enormous computing time, and the current explicit solver should be optimized to balance the computation cost and the numerical stability. Therefore, the current simulation does not include thermal conduction. However, the rise of the flux rope and formation of large-scale CSs are not strongly affected by thermal conduction, because the conduction time $\tau_c = L^2/\kappa$ considering the Spitzer model for κ in corona is generally several orders of magnitude greater than the global evolution time of CMEs. Anisotropic thermal conduction in the corona will be included in the future by developing a new semi-implicit method to save the computation resources.

We set the gravitational acceleration as $\boldsymbol{g} = -g_0\hat{y}/(1 + y/R_\odot)^2$, with the solar radius $R_\odot = 6.961 \times 10^8$ m and the gravitational acceleration near the solar surface $g_0 = 274$ m s^{-2}. Here, $\hat{\boldsymbol{y}}$ is the unit vector in y-direction. Following the work of Isenberg et al. (1993), no CS exists at the very beginning, but only one initial X-point connects to the flux rope and the bottom layer. This X-point collapses into a CS in a short time after the eruption initiates, and the magnetic diffusion outside the CS is negligible so that we only set a uniform resistivity η in a strip covering the CS since its formation. In the simulation, we choose a reference length $L_0 = 10^8$ m and the strip is defined as $(x, y) \in [-0.05L_0, 0.05L_0] \times [p, q]$, where the time-dependent p and q represent the lower and upper ends of the CS. According to the existing numerical experiments of Shen, Lin & Murphy (2011) and Mei et al. (2012), their results showed that the initial electric resistivity or magnetic diffusivity is just used as a triggering required for invoking the tearing mode in the CS, as long as the tearing mode well develops, the dissipation due to the consequent turbulence dominates the diffusion in the sheet. So the initial set-up of the resistivity does not affect the final result significantly. The CS develops with its lower end attached to the bottom flare and is stretched by the motion of the flux rope. Imaging the background magnetic field driven by a quadrupole source buried under the photosphere at a distance d, the pre-existing flux rope is set-up at the initial height h_0 in the corona (see Mei & Lin 2008 for more details).

Following the work of Forbes (1990) for the dipole case, we adopt a smooth distribution of the current density inside the flux rope:

$$j_z(R_-) = j_0 J, \quad 0 \le R_- < (r - \Delta/2) \tag{5}$$

$$j_z(R_-) = j_0 J\{cos[\pi(R_- - r + \Delta/2)/\Delta] + 1\}/2, \quad (r - \Delta/2) \le R_- < (r + \Delta/2) \tag{6}$$

$$j_z(R_-) = 0, \quad R_- \geq (r + \Delta/2), \tag{7}$$

where r is the internal radius, Δ is the width of the shell connecting to the outer region, j_0 is the maximum current density at the centre of the flux rope, J is the intensity of the electric current flowing inside the flux rope in units of I_0, with I_0 the current intensity carried by the flux rope, and $R_- = [x^2 + (y - h_0)^2]^{1/2}$. Otherwise, the use of a uniform profile inside the flux rope as in Nishida, Nishizuka & Shibata (2013) causes a non-negligible error over the thin shell, which eventually leads to a failure in convergence. As a result, the azimuthal component of the flux rope magnetic field B_ϕ is

$$B_\phi(R) = j_0 J R/2, \quad 0 \leq R < r - \Delta/2 \tag{8}$$

$$\begin{aligned} B_\phi(R) = {} & j_0 J\{(r - \Delta/2)^2/2 - (\Delta/\pi)^2 + R^2/2 \\ & + (\Delta R/\pi)\sin[\pi(R - r + \Delta/2)/\Delta] \\ & + (\Delta/\pi)^2 \cos[\pi(R - r + \Delta/2)/\Delta]\}/(2R), \\ & \quad r - \Delta/2 \leq R < r + \Delta/2 \end{aligned} \tag{9}$$

$$\begin{aligned} B_\phi(R) = {} & j_0 J[r^2 + (\Delta/2)^2 - 2(\Delta/\pi)^2]/(2R), \\ & R \geq r + \Delta/2. \end{aligned} \tag{10}$$

To balance the internal equilibrium of the flux rope, we add the axial component of magnetic field within the flux rope B_z so that the flux rope can be force-free. The force-free condition in cylindrical polar coordinates is described as follows:

$$j_z(R_-)B_\phi(R_-) - j_\phi(R_-)B_z(R_-) = 0, \tag{11}$$

where j_ϕ is the azimuthal component of the electric current inside the flux rope. And we have

$$j_\phi(R_-) = -\frac{1}{\mu}\frac{dB_z}{dR_-}. \tag{12}$$

Then it follows that

$$B_z(R_-) = \sqrt{2\mu \int_{R_-}^{+\infty} j_z(R)B_\phi(R)dR}, \tag{13}$$

where B_z functions as a guide field confined in the radius of the flux rope.

The initial configuration and the boundary conditions are as follows. The background magnetic field is driven by a quadrupole source underneath the photosphere at a depth of $d = 0.4L_0$ with a strength $125\sigma\mu I_0/(96\pi)$, where the background relative strength is $\sigma = 0.8$ and the current intensity I_0 is given from the predefined j_0J in equations (5–7). The initial height of the pre-existing flux rope is given as $h_0 = 0.61d$ with a critical radius of $r_0 = 0.15d$, which allows for a catastrophic eruption (see the detailed equilibria analysis in Forbes 1990; Mei & Lin 2008). Note that the CS does not exist at the very beginning, but its formation is determined by the motion of the flux rope. The expressions for the magnetic field including the pre-existing flux rope in our simulation are described by the following equations,

$$\begin{aligned} B_x = {} & -B_\phi(R_-)(y - h_0)/R_- + B_\phi(R_+)(y + h_0)/R_+ \\ & + B_\phi(r + \Delta/2)Md(r + \Delta/2)(d + y)(3x^2 - (y + d)^2)/R_d^6, \\ B_y = {} & B_\phi(R_-)x/R_- + B_\phi(R_+)x/R_+ \\ & + B_\phi(r + \Delta/2)Md(r + \Delta/2)x(-x^2 + 3(d + y)^2)/R_d^6, \end{aligned} \tag{14}$$

where

$$\begin{aligned} \Delta &= 0.025d, r = r_0 - \Delta \\ R_+^2 &= x^2 + (y + h_0)^2 \\ R_d^2 &= x^2 + (y + d)^2 \\ M &= \frac{125\sigma}{32}. \end{aligned}$$

In the above equations, the terms R_+ and R_d originate from its mirror image below the photosphere and the quadrupole source, respectively.

The simulation domain is $(x, y) \in [-4L_0, 4L_0] \times [0, 14L_0]$, in which $y = 0$ represents the photosphere, and the whole domain covers approximately $2R_\odot$ beyond the solar surface. The initial density set-up near the bottom is specified to hold approximately the boundary condition, because the line-tied boundary condition utilized at the lower boundary is too complicated to be satisfied analytically as described in Forbes & Priest (1984). We adopt instead a very high density in the two thin layers below the corona with the depths $h_p = h_c = 1 \times 10^6$ m to satisfy the stratification following the work of Forbes (1991), which in turn decreases the cost of the calculation significantly. The temperature at the base of corona (i.e. $y = h_p + h_c$) is given as $T_c = 1.0648 \times 10^6$ K, while the temperature at the photosphere is set to $T_p = 4300$ K when $y \leq h_p$ (the lowest value in fig. 9 of Linsky & Avrett 1970). We eventually treat the temperature in the transition region ($h_p \leq y \leq h_p + h_c$) by a simple interpolation as Mei et al. (2012) as well as the density distribution. Note that, in the practical simulations, we also execute a static mesh refinement (SMR) of maximumly four levels to maintain the steep density gradient in this particular region. Four successive layers are initially set-up before the computation starts: level 1 for $y \leq 0.04L_0$, level 2 for $y \leq 0.03L_0$, level 3 for $y \leq 0.02L_0$, and lastly level 4 for $y \leq 0.01L_0$. Then, we describe the plasma density distribution in the corona following the S&G model (Sittler & Guhathakurta 1999). It takes the form of $\rho(y) = \rho_0 f(y)$, where ρ_0 is the reference density and $f(y)$ is a dimensionless function of the height y (in units of the solar radius) given by

$$f(y) = a_1 z^2(y)e^{a_2 z(y)}[1 + a_3 z(y) + a_4 z^2(y) + a_5 z^3(y)], \tag{15}$$

where $z(y) = 1/(1 + y)$, $a_1 = 0.001292$, $a_2 = 4.8039$, $a_3 = 0.29696$, $a_4 = -7.1743$, $a_5 = 12.321$, with $f(0) = 1$. Consequently, the gas pressure is computed by

$$p(y) = p_c - \int_{h_p+h_c}^{y} \rho \mathbf{g} \mathrm{d}y. \tag{16}$$

Here, we have $p_c = 2\rho[(h_p + h_c)/R_\odot]T_c k_B/m_H$, the Boltzmann constant $k_B = 1.38 \times 10^{-23}$ erg K^{-1}, the mass of the hydrogen atom $m_\mathrm{H} = 1.67 \times 10^{-27}$ kg. Note that the pressure also includes electrons.

Additionally, the work of Mackay & van Ballegooijen (2009) points out that the flux rope consists of cold filament material coming from the chromosphere, which is isolated from the hot corona by a thin transition shell. Without losing generality, we simply set a constant cool temperature in the internal radius and a smooth distribution in the outer shell of the flux rope to avoid the unexpected sharp discontinuity as follows:

$$T(R_-) = T_f, \quad 0 \leq R_- < (r - \Delta/2) \tag{17}$$

$$\begin{aligned} T(R_-) = {} & (T_\mathrm{amb} - T_f)(R_- - r + \Delta/2)/\Delta + T_f, \\ & (r - \Delta/2) \leq R_- < (r + \Delta/2) \end{aligned} \tag{18}$$

$$T(R_-) = T_{\rm amb}, \quad R_- \geq r + \Delta/2, \tag{19}$$

where $T_f = 5 \times 10^4$ K and $T_{\rm amb}$ is the ambient temperature surrounding the flux rope obtained according to the ideal gas law.

In order to further study the fine structure responsible for the cascading reconnection and energy conversion inside the CS during the solar eruption, we use a uniform root grid of 800 × 1400 and the AMR refinement of seven levels in the vicinity of the CS. This yields the largest grid size of $\Delta x = \Delta y = 0.01L_0$ and the smallest grid corresponding to a length of 7.5 km.

Another important improvement includes the method for the open boundary condition implementation along the three sides excluding the bottom ($y = 0$). One can find the theoretical description of an open boundary in the work of Forbes & Priest (1984) through which the magnetic field and the plasma can enter or exit freely. By convention, people are used to approximating this condition with a simple extrapolation method, more particularly the 'outflow' condition, to abstain from the computational complexity. However, the simple extrapolation boundary condition may cause unphysical wave reflection at the boundary, and the use of the 'outflow' condition will cause small error near the boundary. Orlanski (1976) also mentions that the boundary could produce a substantial effect on the system as the moving MHD waves or the magnetic bubble surrounding the flux rope approach the boundary. In our numerical experiments, we observed that the flux rope was obstructed by the outflow boundary. A larger simulation domain may reduce the impact of the boundary, but the flux rope will stop and fluctuate at a certain height which is still far away from the top. To solve that problem, we made a simple extrapolation in a sense of zero gradient over the magnetic potential instead of magnetic field so that the flux rope can propagate through the boundary successfully.

For the parameter study of this model, we launched two simulations with different values of the electric current density inside the flux rope j_0J in equations (5–7), which yields the initial magnetic fields of different strengths. The reference density ρ_0 is 1.67×10^{-11} kg m^{-3} at the surface of the Sun and we add a uniform resistivity $\eta = 5 \times 10^8$ m^2 s^{-1} in the strip defined above, eventually leading to different Lundquist numbers $S = V_{FR}h_0/\eta$, where V_{FR} is the initial Alfvén velocity at the centre of the flux rope. The locations p and q are taken as fitting functions obtained by performing the same simulation several times. Thus, the resistive diffusion time is calculated as $\tau_d = L_0^2/\eta = 5.56 \times 10^3$ h (for the characteristic length L_0). The kinematic viscosity, ν, is also set to be uniform with a value of 1×10^8 kg m^{-1} s^{-1}, and it corresponds to a viscous diffusion time, $\tau_\nu = L_0^2/\nu$, or $5\tau_d$. The domain of AMR is also confined in a strip covering the CS defined as $(x, y) \in [-0.2L_0, 0.2L_0] \times [p, q]$, rather than the entire simulation volume, to save computational resources, because the complex geometry and small-scale events inside the CS are what we care about the most in this work. Run A and Run B correspond to different p and q as reported in Table 1. Fig. 1(a) shows the initial magnetic configuration for both runs. Before performing the numerical experiments, it is appropriate to pay serious attention to the numerical diffusion when the AMR is used. As we know, the accumulated error can introduce false electric currents. If they become substantial compared with the physical current, it causes erroneous estimation of the geometry of the CS and its reconnection rate. To estimate the effect of numerical diffusion, we rewrite the magnetic induction equation by adding an extra diffusion term as follows.

$$\partial_t \boldsymbol{A} - \boldsymbol{v} \times \boldsymbol{B} + \eta \nabla \times \boldsymbol{B} = \eta_n \nabla \times \boldsymbol{B}, \tag{20}$$

where η_n is the equivalent numerical diffusivity.

We notice that the magnetic potential $\boldsymbol{A}$ is calculated by integrating the magnetic field $\boldsymbol{B}$ at the given time, and the integration originates at a fixed point (normally on the boundary) far from the interesting area with an initial value $\boldsymbol{A}_0$ of zero at this point. This allows the resulting magnetic potential terms $\boldsymbol{A}$ to be comparable on the same frame, and hence the term $\partial_t \boldsymbol{A}$ is deduced by the finite difference method. Fig. 1(b) plots the averaged ratio η_n/η in a vicinity of the PX-point from $t = 270$ to $t = 800$ s computed from the outputs using seven levels of AMR for Run A. As shown on the plot, its percentage starts at 12 per cent, and drastically falls off to 4 per cent, then trends to be flat around 2 per cent afterwards. The explanation is based on the fact that the use of AMR with a maximum of seven levels does not reach the highest level immediately. When the structure inside the CS becomes more complex, the computation needs to utilize the finer resolution to capture it. The plateau of this curve indicates that the finest resolution is reached and the amplitude of the ratio is of the order of 2 per cent, which is ignorable in the computation. In other words, numerical diffusion does not strongly affect the physical results in the area of interest. The entire simulation was performed on Milkeyway-2 supercomputer centre in Guangzhou employing 480 CPUs in an MPI–open-MPI parallel environment.

3 SIMULATION RESULTS

In this section, we compare the global evolution of the flux rope eruption for Runs A and B as well as the dynamical features inside CS responsible for the energy conversion when magnetic reconnection occurs. As we know, the difference between Run A and Run B lies in the maximum current density j_0J, which yields the magnetic field of about 120 and 240 G at the origin, respectively.

3.1 Global evolution

The snapshots in Fig. 2 show the time evolution of the mass density on a log scale in Run A and Run B. The top panels are for Run A at different flux rope heights $h_{FR} = 2 \times 10^8$, 5×10^8, 8×10^8 m, and the bottom panels are for Run B at the same heights. The upward reconnection jets collide with the ejected flux rope to form a high-density envelope below the CME, while the downwards reconnection jets collide with the closed magnetic field to form the flare loops at the bottom. At $h_{FR} = 2 \times 10^8$ m, a fast shock is formed by the motion of the flux rope. Run A generates a fast shock of 350 km s^{-1} near the borders, while Run B has a fast shock of 800 km s^{-1} which does not touch the borders yet. The global current layer connecting the flux rope and the flare loops forms a Y-structure at an early stage. At $h_{FR} = 5 \times 10^8$ m, a dimming region between the fast shock and the CME edge is formed, and a high-density shell is observed around the flux rope due the accumulation of the plasmoids ejected from the reconnecting CS. The shell, the flux rope, and the region in between constitute the so-called three components of CMEs. At $h_{FR} = 8 \times 10^8$ m, Run B displays another conspicuous dimming region over the flare loop, while Run A does not. This phenomena can only be found in our numerical tests for the moderate or fast CMEs, because the CS shrinks so quickly that there is no time to replace the mass transported into the CS via magnetic reconnection. One can also notice that the fine structure

Table 1. Simulation parameters for Runs A and B. Here, j_0J is the current inside the flux rope, S is the Lundquist number, p and q are lower and upper ends of the CS.

	j_0J(A m^{-2})	$S = h_0V_{FR}/\eta$	p (m)	q (m)
Run A	0.974×10^{-2}	1.18×10^5	2.5×10^6	$4.08 \times 10^6 + 4.65 \times 10^4t + 23.34t^2$
Run B	1.948×10^{-2}	2.35×10^5	2.5×10^6	$9.3 \times 10^6 + 1.13 \times 10^5t + 70.563t^2$

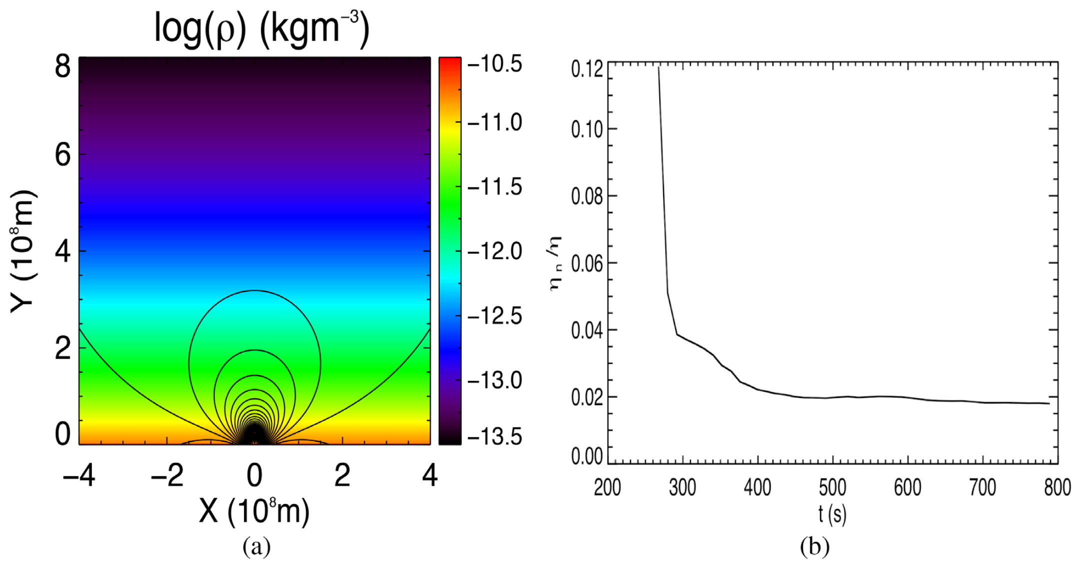

Figure 1. (a) Distribution of the initial magnetic field and mass density in the simulation domain. (b) Ratio of the numerical diffusivity η_n to the physical one η versus time.

of CS for Run B is more turbulent for Run A due to the higher Lundquist number in the vicinity of CS.

In Fig. 3, we show the time-distance plots of density ρ on a log-scale along $x = 0$ line in Runs A and B. From that figure, we use an automatic diagnosis to track several characteristic variables. The fast shock and CME leading edge are detected as sharp changes in the mass density, between which there is a dimming region. The centre of the flux rope has the maximum mass density of the cool material along the central line $x = 0$ in the corona. The termination shocks towards the CME and sunward are detected as the discontinuities of v_y as shown in Fig. 4. The principal X-point is identified as the location where the magnetic flux changes the fastest in CS. By these methods, we are able to follow the dynamic features appearing in the entire simulations, which are generally consistent with the flare model (Reeves & Forbes 2005; Forbes et al. 2018). The red line in Fig. 3 corresponds to the position of the core of flux rope. We observe surprisingly that Run A presents a sigmoid behaviour with two turning points at about $t = 1000$ and $t = 3000$ s, as does the CME leading edge. The separated region between the flux rope and the CS consists of a thin layer of the hot and dense plasma that oscillates due to non-symmetric outflow jets. When the region becomes turbulent because of the compression between the ejected plasmoids and the CME, multiple magnetic islands merge into a large one via reconnection and heat the plasma again. The lower end of the CS is attached to the flare loops with the termination shock and alternating plasmoid oscillations in between. High-density plasma blobs start to appear at $t = 220$ s for Run A and $t = 100$ s for Run B, being ejected from the CS. In Run A, we calculate the length of the CS L_{CS} right before the first plasmoid's appearance by differentiating the positions of the upper and lower tips of the CS as well as the width δ_{LS} by measuring the half-height current across the PX-point. They are $L_{CS} \approx 1.15 \times 10^4$ km and $\delta_{CS} \approx 90$ km. This indicates that the aspect ratio of CS $L_{CS}/\delta_{CS} \approx 127.8$ for the onset of the tearing mode. As time goes on, more and more plasmoids appear in the global layer and frequently collide with each other before being ejected from the CS. This fact is important to improve the understanding of the intermittency of the magnetic reconnection speed. We also notice that the principal X-point (solid line) is located near the bottom end of CS during the entire eruption for both runs, causing the energy partition to be unequal. The development of plasmoids is seen more clearly in the time-distance diagram of the vertical velocity v_y along the $x = 0$ line zooming in $[0, 6 \times 10^8]$ for both runs as shown in Fig. 4. In Run A, the upper outflow has an average speed of $v_y \approx 1258.3$ km s^{-1}, while the average sunward speed is $v_y \approx 723$ km s^{-1}. In Run B, the corresponding upwards speed is $v_y \approx 2345.4$ km s^{-1} and the sunward one is $v_y \approx 944.5$ km s^{-1}. We notice that the upper and lower outflows are not symmetric. The kinetic energy available in the upper outflow is generally much larger than the lower one. In addition, we calculate the typical Mach number at the shock front for Run A, which gives $M_A = 3.75$ for the upper termination shock and $M_A = 1.80$ for the lower termination shock, respectively. The modest Mach numbers are important to understand the properties of termination shocks, especially since shocks below Mach numbers of about 2.7 are likely to be sub-critical and may not accelerate particles efficiently. That is very consistent with the Mach number for a solar flare termination shock given by both observations and simulations (Chen et al. 2015).

To compare with CMEs in the corona, we plot the rising velocities of the flux rope as functions of height for both runs in Fig. 5. The green dashed line presents the rising speed in the range 100–240 km s^{-1} for Run A, while the blue solid line gives the speed

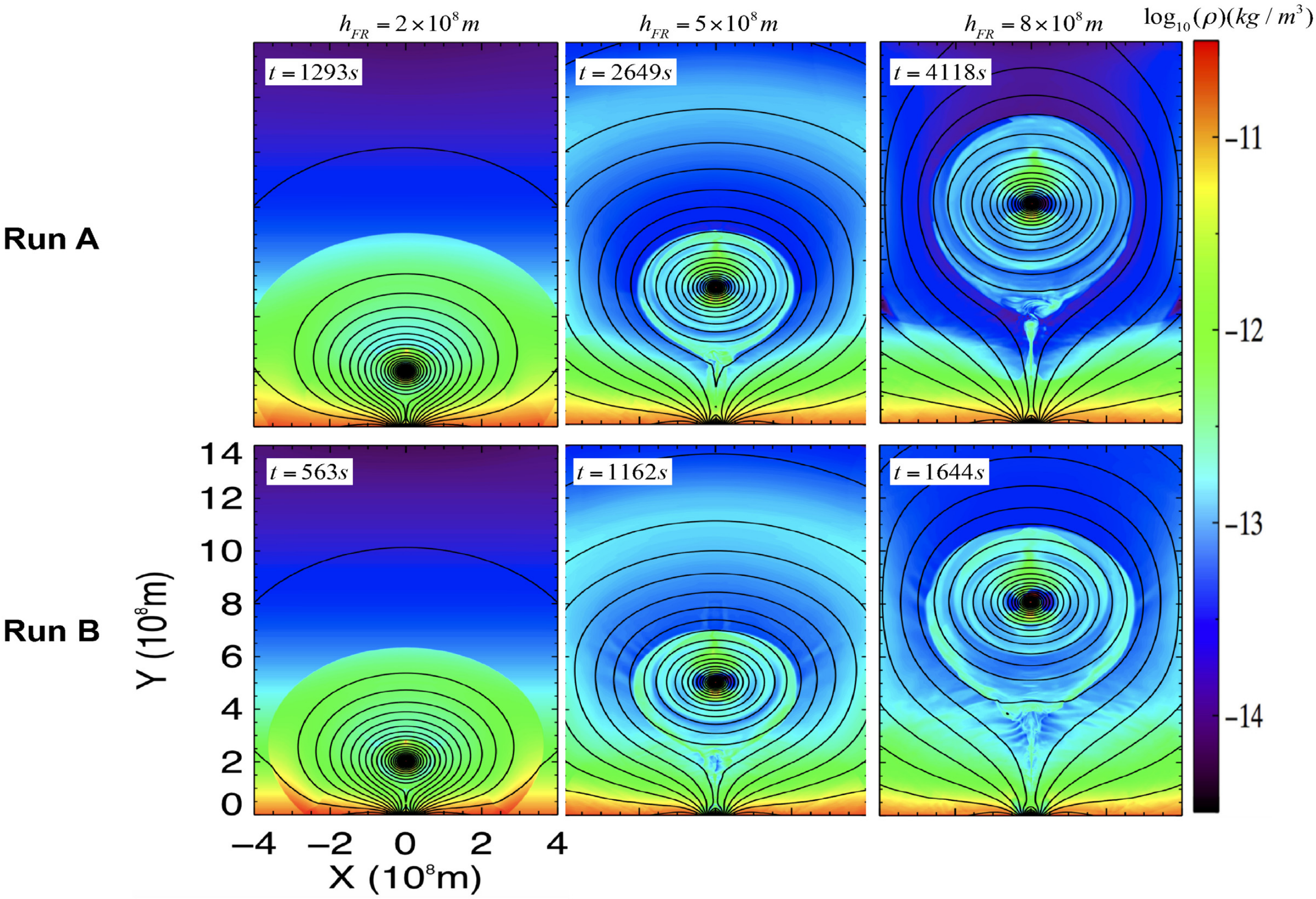

Figure 2. Snapshots of the magnetic field and the coronal mass density at different heights for both Run A and Run B.

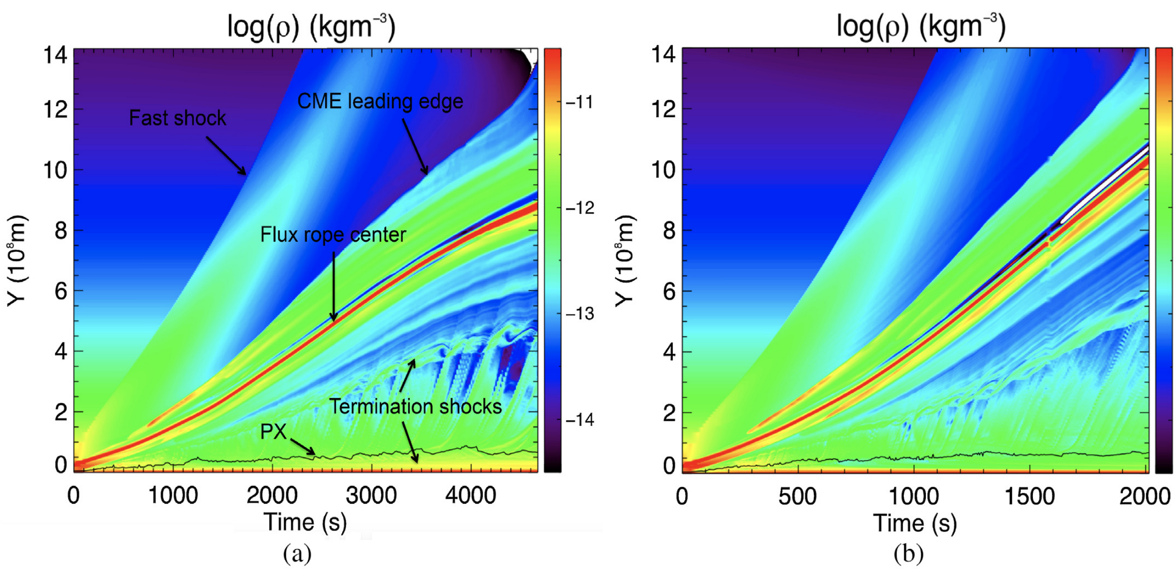

Figure 3. Time evolution of the mass density along $x = 0$. (a) Run A. (b) Run B.

ranging from 240 to 660 km s^{-1} for Run B. Recently, Song et al. (2018) studied the C1.1 flare on 2011 December 25 with AIA and Helioseismic and Magnetic Imager (HMI) data, and they analysed the contributions of non-equilibrium instability and magnetic reconnection responsible for the two stages of acceleration. Their results are consistent with our Run B, which shows also two stages of acceleration under 1 R$_\odot$. Since the flux rope is able to escape smoothly from the top boundary at the end of both runs, reconnection is proven to be fairly efficient to drive the eruption. The reasonable explanation is that the magnetic field for Run A is too

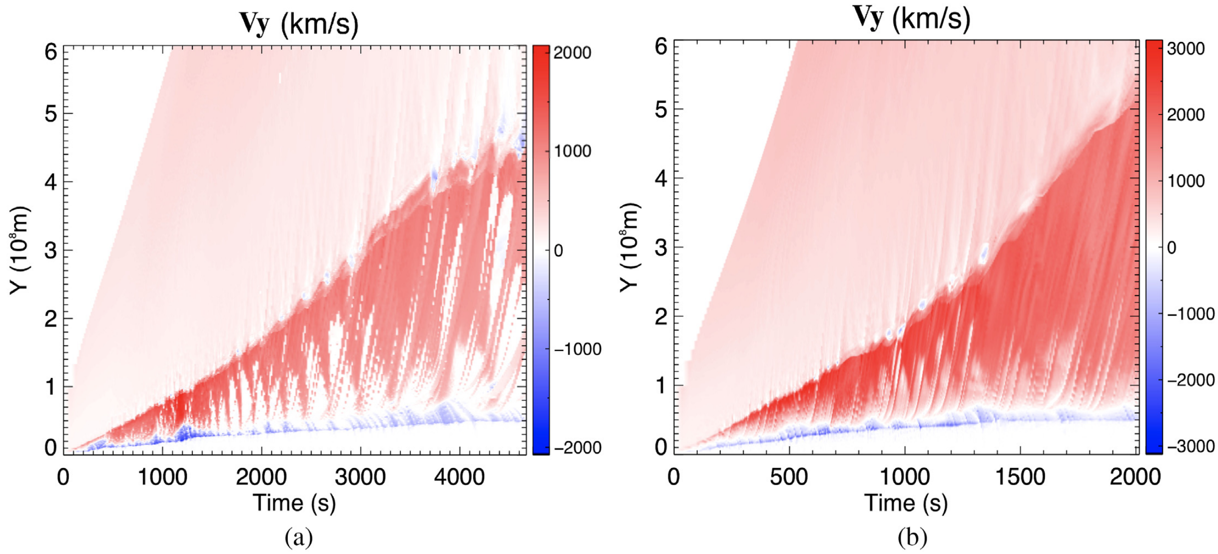

Figure 4. Time-distance diagram of v_y along the $x = 0$ line. (a) Run A. (b) Run B.

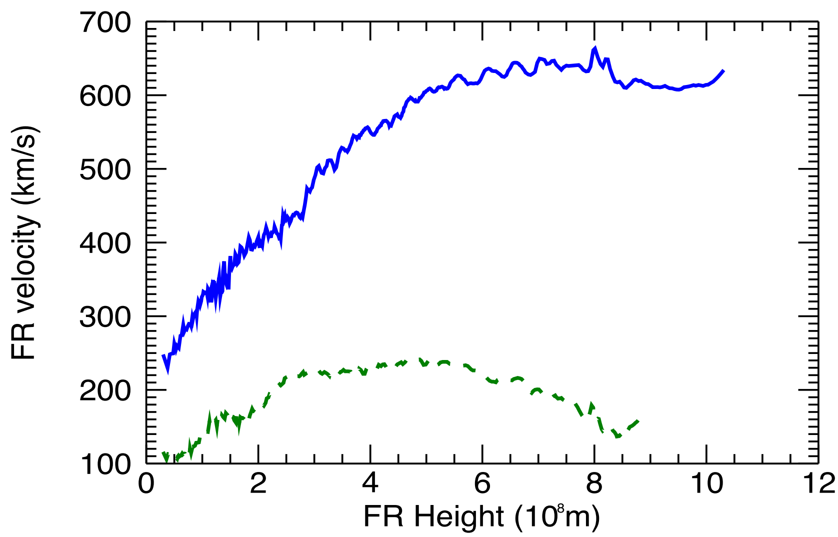

Figure 5. Comparison of the flux rope rising velocities versus height for both Run A (green dashed line) and Run B (blue solid line).

weak (<27 G on average at the low corona) to overcome gravity in this model, which does not meet the minimum strength required in the calculation of Lin (2002). However, a stronger background magnetic field generates a faster CME from the same non-equilibrium state, but the general dynamical properties of slow and fast CMEs show no difference in agreement with Svestka (2001).

3.2 Energy dissipation and spectrum study

In this section, we consider the energy integral for specific regions of interest to quantify the various energy flows. By integrating both sides of equation (2) over the specified volume and applying the divergence theorem, we get the following expression:

$$\int \frac{\partial}{\partial t}(\mathcal{E}+\mathcal{K}+\mathcal{W}) = \int (\rho \boldsymbol{v}\cdot \boldsymbol{g})\mathrm{d}V - \int \left[\left(\frac{\gamma p}{\gamma - 1} + \frac{\rho v^2}{2}\right)\boldsymbol{v} + \frac{1}{\mu}\boldsymbol{E}\times\boldsymbol{B} + \boldsymbol{v}\tau \right]\cdot \mathrm{d}\boldsymbol{S}, \qquad (21)$$

where $\mathcal{E}$, $\mathcal{K}$, and $\mathcal{W}$ are the internal, kinetic, and magnetic energy densities. The energy is dissipated via reconnection to allow for a successful escape. In the absence of reconnection and energy dissipation, the flux rope will be trapped and oscillate at an upper equilibrium altitude. Firstly, we calculate the dissipated magnetic energy E_m, the kinetic energy E_k, the generated thermal energy E_i and their ratio E_k/E_m over the entire simulation domain as functions of the height of flux rope for both runs for a general comparison. Since open boundaries are used, the system is not isolated, and substantial energy flows through the upper boundary. Here, the magnetic, kinetic, and thermal energy flowing into the simulation volume through the upper open boundary from the beginning ($t = 0$) to time t is denoted by E_{MF}, E_{KF}, and E_{TF}, respectively (note that these quantities may have negative signs if energy flows out of the simulation volume). The magnetic, kinetic, and thermal energy confined in the full volume at time t are denoted by E_{ML}, E_{KL}, and E_{TL}. Accordingly, the initial magnetic, kinetic, and thermal energy is denoted by E_{MI}, E_{KI}, and E_{TI}, respectively. As a result, we obtain the relationship $E_m = E_{MI} + E_{MF} - E_{ML}$, $E_k = E_{KL} - E_{KF} - E_{KI}$, and $E_i = E_{TL} - E_{TF} - E_{TI}$ for the above notations. The detailed calculations for the mentioned quantities are similar to those in Ni et al. (2012b).

As shown in Fig. 6, the dissipated magnetic energy in the left-hand panel on the top manifests generally in a piecewise linear phase with the only turning point at $y \approx 3 \times 10^8$ m, which corresponds to the two stages of acceleration found in Fig. 5. The right-hand panel on the top shows the kinetic energy converted from the magnetic energy, which reveals an accumulation of the kinetic energy below $y \approx 2 \times 10^8$ m, and then a smooth decay afterwards. The left-hand panel at the bottom shows the generated thermal energy, which shows a quasi-linear regime versus the height of the flux rope. Thanks to the high-resolution grids used in our simulations and conservative numerical schemes with low diffusion of the code, the dissipated magnetic energy equals almost the sum of the kinetic energy and the generated thermal energy; the errors are under 1 per cent due to the numerical dissipation. Although the energy flows (magnetic, kinetic) for Run B are several times greater than Run A, the percentage curves of the kinetic energy versus the dissipated magnetic energy are very similar as shown in the right-hand panel at the bottom. Indeed, according to our calculation, even in the accumulation phase of the kinetic energy at least half of the dissipated magnetic energy goes into heating the plasma (here, we ignore the contributions to particle acceleration and wave energy at MHD scales). Until the end, the kinetic energy ratio is within 10 per cent for Run A and 20 per cent for Run B, respectively. In other words, most of the magnetic energy is converted into the thermal energy during the dynamic process of CMEs.

In order to determine the details of the energy conversion mediated by plasmoid instability in the CS during the CME eruption, we set an initial volume with the size of $2000 \times 6000\,\mathrm{km}^2$, whose top and bottom are the upper and the lower ends of the CS (see Fig. 7a), following the entire CS since its formation in Run A . The length of the volume changes with upper and lower tips of the CS when stretched by the motion of the flux rope. The Poynting flux $\int \boldsymbol{E} \times \boldsymbol{B}/\mu \cdot \mathrm{d}\boldsymbol{S}$, the enthalpy flux $\int [\gamma p/(\gamma - 1)]\boldsymbol{v} \cdot \mathrm{d}\boldsymbol{S}$, the kinetic energy flux $\int (\rho v^2/2)\boldsymbol{v} \cdot \mathrm{d}\boldsymbol{S}$ and the viscosity flux $\int \tau \boldsymbol{v} \cdot \mathrm{d}\boldsymbol{S}$ that flow across the control volume are computed by integrating along the associated boundaries. Fig. 7(b) shows the different components of energy that flow across the inflow boundaries. The Poynting flux dominates during the entire eruption, while the kinetic energy flux and enthalpy fluxes are one or two orders of magnitude smaller than the Poynting flux in the early stages, then converge to the same order later. In Fig. 7(c), the bulk energy flow at the upper outflow is due to the kinetic energy flux, and the enthalpy flux is nearly one order smaller. In Fig. 7(d), we can observe that the enthalpy flux is slightly greater than the kinetic energy flux at the lower outflow. The kinetic energy flux is available for conversion to thermal energy at the termination shock to heat the plasma in the quasi-stationary flare loops. Comparing the Poynting flux in Figs 7(b–d), one can find evidence that 99 per cent of the magnetic energy coming from inflow region is converted to other sorts of energy by magnetic reconnection. The viscous flux is not shown because it is several orders of magnitude smaller than the others.

Looking into the energy distribution of magnetic islands in the time evolution of the CS, we perform a 1D spectral analysis along the CS ($x = 0$ line) for the magnetic energy using the Fourier transform method for Run A. The left column of panels in Fig. 8 shows the distribution of the B_x component of magnetic field, averaged along x-axis, in a strip covering the evolving CS as well as the bottom flare loops five cells wide at the AMR refinement level 5 for times $t = 505.29$, $t = 998.036$, and $t = 2001.02$ s. The negative peak located near the bottom boundary in the black lines is identified as the flare loops enclosed by the magnetic field, and the null points on the right side indicate small-scale magnetic islands or plasmoids within the CS. One can also notice the significant bumps between the termination shock and the flare, which yield many small-scale magnetic islands as reported in the work of Takahashi, Qiu & Shibata (2017) and Jelínek et al. (2017) recently. The right column of panels in Fig. 8 are obtained by applying the Fourier transform to the previous E_m to plot the magnetic power spectrum as a function of wavenumber k. As we know, the greater k is the smaller scale structure it represents. We follow all the magnetic islands in the developed CS driven by the motion of the flux rope at different evolution stages and fit their spectra using a power law. We fit the spectrum using the function $E = a_0 k^{-\gamma}$ on doubly logarithmic axes with identical error bars over the k range for the quasi-linear phase. The solid line in Fig. 8(b) gives the discretized result from the Fourier transform at time $t = 505.29$ s and the red straight line indicates the magnetic spectrum index γ_m obtained by linear regression. In this stage, magnetic islands develop smoothly in the outflow direction and the spectrum distribution is dominated by a single power law of index 1.63. Fig. 8(d) shows the situation at $t = 998.036$ s and the spectral index is 2.05, as the distribution starts to become steep due to the growth of large plasmoids. The energy now mainly cascades to large scales. In the later stage of Fig. 8(f), the magnetic spectrum no longer follows a single power law, but more a gradual rollover of slopes. Accordingly, the spectral indices are 1.83 for the inertial range ($1 < k < 1000$) and 5.10 for the dissipation range ($k > 1000$), respectively. We have also checked that the increasing profile for $k > 2000$ is mainly related to the small-scale islands resulting from the interaction between the flare and the termination shock. Note that the magnetic spectrum here is more flattened compared to that of Fig. 8(d) because of the appearance of secondary islands (Ni et al. 2012a; Ni, Lin & Murphy 2013), and magnetic islands engage in a steady cascading reconnection process.

The fact is that the energy transfer ends at $\approx$200 km (or $k \sim 1000$) in Fig. 8(f), which is understood as the turning point between the inertial range and the dissipative range and the smallest recognizable CSs in this model. The typical width of the dissipative CS now is $L_d = 52.9$ km as given by the full-width at half maximum of the current density horizontally across the principal X-point. Some numerical work suggests that the plasmoid dimensions along the CS are one order (typically $\times 6$) larger than that across the CS (Bárta et al. 2011), the dissipation scale of the magnetic energy along the CS is thus $\approx 6L_d = 300$ km, which is already attained in Fig. 8(f). The distribution of the Fourier spectrum reveals the filamented CSs between plasmoids embedded within the global CS layer.

On the other hand, the evidence of dissipation at macroscales does exist in the induction equation. By ignoring the effect of the fluid movement, equation (4) reduces to $\partial_t \boldsymbol{B} = \eta \nabla^2 \boldsymbol{B}$ with η constant. So the energy dissipation is also related to the change of the magnetic field in space, and it reveals approximately $\tau_d = l_c^2/\eta$. In Run A, the typical diffusion time for plasmoid coalescence processes is considered as the average full time of two plasmoids merging over $\tau_d \approx 120$ s, thus the characteristic length for dissipation is $l_c \approx 245$ km with η used in Section 2. Both numerical experiments and theoretical arguments state that dissipation starts at scales much larger than kinetic scales.

Forbes et al. (2018) recently points out that outflow jets accelerate only in the single diffusion region of the principal X-point and then propagate at a constant speed in the advection region of the global CS. Unlike his work, the existence of cascading plasmoids found in

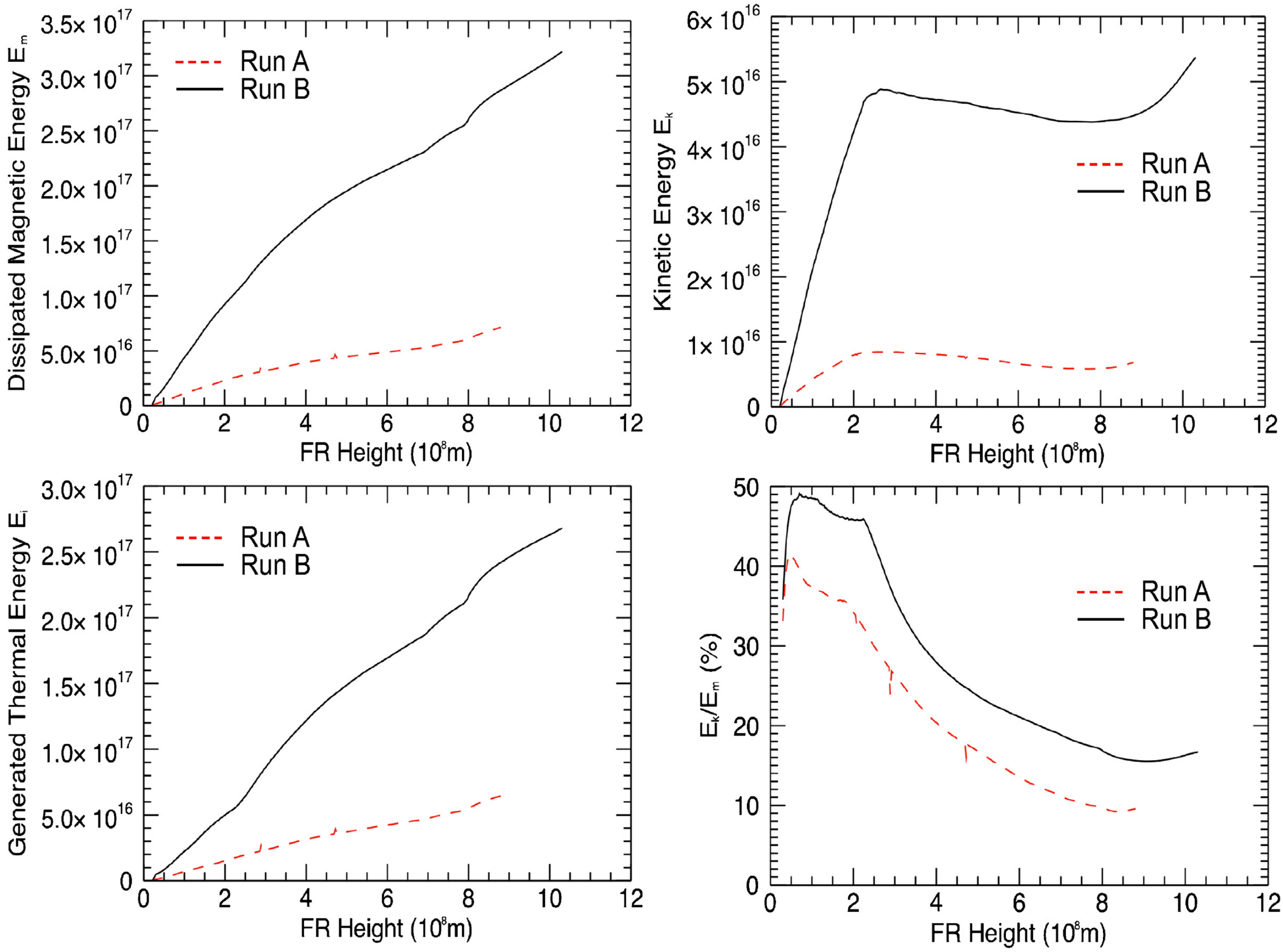

Figure 6. Dissipated magnetic energy E_m, kinetic energy E_k, generated thermal energy E_i and their percentage E_k/E_m(per cent) versus height for both Run A and Run B over the entire simulation box.

our simulations provides many acceleration regions which enlarge greatly the diffusion region. In Fig. 9, we have the distributions of the outflow velocities at $t = 213.16$, 998.036 s, and the blue X is the location of the principal X-point. R1 and R2 enclosed by red dashed lines represent the diffusion region and the advection region, respectively. The left-hand panel shows the result for $t = 213.16$ s, and the outflow jets at both sides of the principal X-point accelerate from 0 to almost 1000 km s^{-1} only in the diffusion region just before the first plasmoid appears. Then outflow velocities are stopped by termination shocks outside R1. The right-hand panel presents the situation at $t = 998.036$ s, the fact is that the outflow jets accelerate not only in the diffusion region, but also decelerate and accelerate intermittently in the advection region, the entire CS consists of many small-scale diffusion regions because of the cascading plasmoids. Similarly, the outflow velocities are stopped by termination shocks outside R1 and R2.

3.3 Fragmentation and cascading

The fragmentation happens everywhere within the global current layer due to the tearing mode instability, and the energy cascades from the large scale to the small scale via plasmoids. The fragmented CSs provide multiple non-ideal regions where the dissipation can take place, when plasmoids are subject to both separation and coalescence. During the simulation, a number of plasmoids are generated through magnetic reconnection. Some plasmoids merge into bigger ones and move along the CME direction and sunward, and eventually accumulate in the flux rope and flare loops. Figs 10(a) and (b) show the mass density distribution and the velocity field at the bottom of the flux rope and near the cusp structure of the flare at $t = 4283$ s. They present different patterns of turbulence at two ends of the global CS. At the top end, the ejected plasma accumulates into a high-density turbulent region that oscillates underneath the flux rope. The plasma from the outflow jets is dragged by the gravity to float between the CS and the flux rope, then the subsequent jets crash into it to make the gas even hotter by compression and push the mass to the top of the flux rope. At the lower end, the turbulent gas only concentrates on the top of flare loops for a short time before it is ejected downward along the loops to form a dense shell. Meanwhile, their associated current density distributions (Fig. 10c,d) represent the so-called turbulent reconnection and the resulting CSs inside. In order to study the general impact on reconnection efficiency dominated by cascading reconnection and subsequent fragmentation of the CS, we follow the merging of a group of plasmoids from $t = 4082$ to $t = 4540$ s in the 40–160 Mm interval for Run A. In Figs 11(a–c), we show zoom-ins of the current density and velocity field for time $t = 4091$, 4106, and 4125 s, respectively, to follow a complete merging process of two

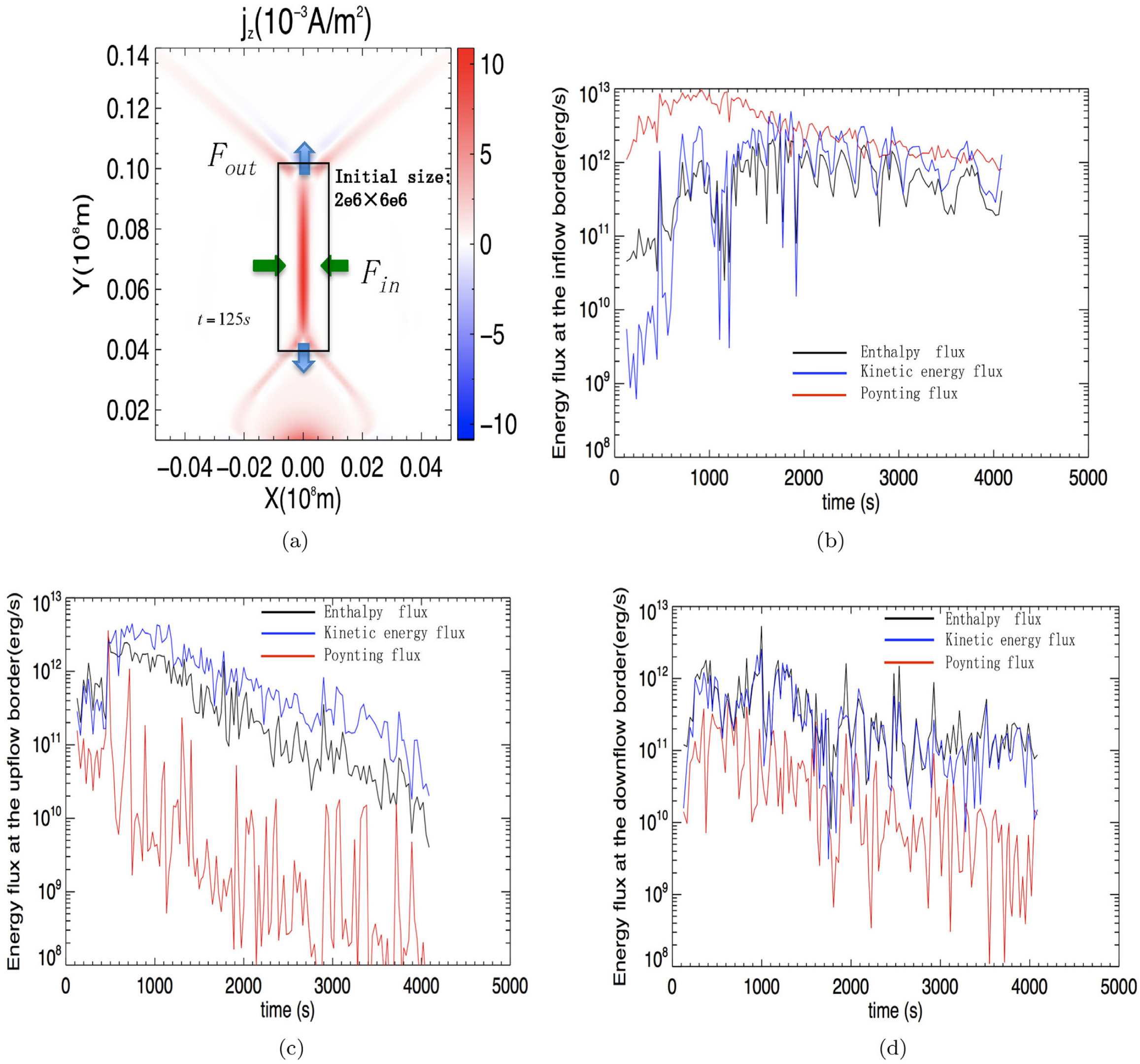

Figure 7. Time evolution energy fluxes around a size-changing box covering the CS for Run A.

individual plasmoids mediated by cascading reconnection. At time $t = 4091$ s (Fig. 11a), they start to merge into one larger plasmoid between which their X-point collapses smoothly. At $t = 4106$ s (Fig. 11b), a CS of opposite polarity perpendicular to global current layer then appears and the plasmoid above inverts its sense of propagation to interact with the one below. At time around 4125 s (Fig. 11c), the merging is almost complete and smaller pieces of current layers appear inside the larger merged plasmoid. We plot also the current density along the dashed y-direction line which crosses the X-point at the beginning of coalescence. In Fig. 11(d), the X-point is located near the largest peak with a positive valued $j_z \approx 1.3 \times 10^{-2}$ A m^{-2}. Then Fig. 11(e) indicates the opposite behaviour at the cascading spot, where $j_z \approx -1.5 \times 10^{-2}$ A m^{-2}. At the end of merging in Fig. 11(f), there exist still several fragmented CSs within the large plasmoid, where even smaller scale events take place. The fact is that the whole lifetime for a typical event of double plasmoids merging can last over 34s (≈0.5 per cent of the simulation time) and such events are happening at any time once the global current layer reaches the tearing mode instability, at places such as the bottom of the flux rope, the magnetic arcade and sometimes within the CS. That definitely has an important impact on reconnection efficiency.

To study the general reconnection dynamics in the global CS layer, it is worth tracking all the magnetic nulls continuously. To identify the neutral points, we develop an automatic diagnosis method by examining the Hessian matrix (Rana 2004) with the second-order partial derivatives of the magnetic potential A, defined as

$$H_{ij}(\boldsymbol{x}) = \frac{\partial^2 A}{\partial x_i \partial x_j}, \tag{22}$$

where x_i, x_j are either x or y. Conventionally, we locate the distribution of magnetic nulls using $\nabla A = 0$ and then compute the eigenvalues of H_{ij} to determine the properties of each critical point. In our simulations, these points are non-degenerate critical points, whose Hessian matrix has two non-zero eigenvalues. If the Hessian has both positive and negative eigenvalues, then $\boldsymbol{x}$ is an X-point; otherwise, it is an O-point. Our interest is in the complex magnetic topology when plasmoids coalescence, and critical points could be very close to each other. Although we use the highest level (=7)

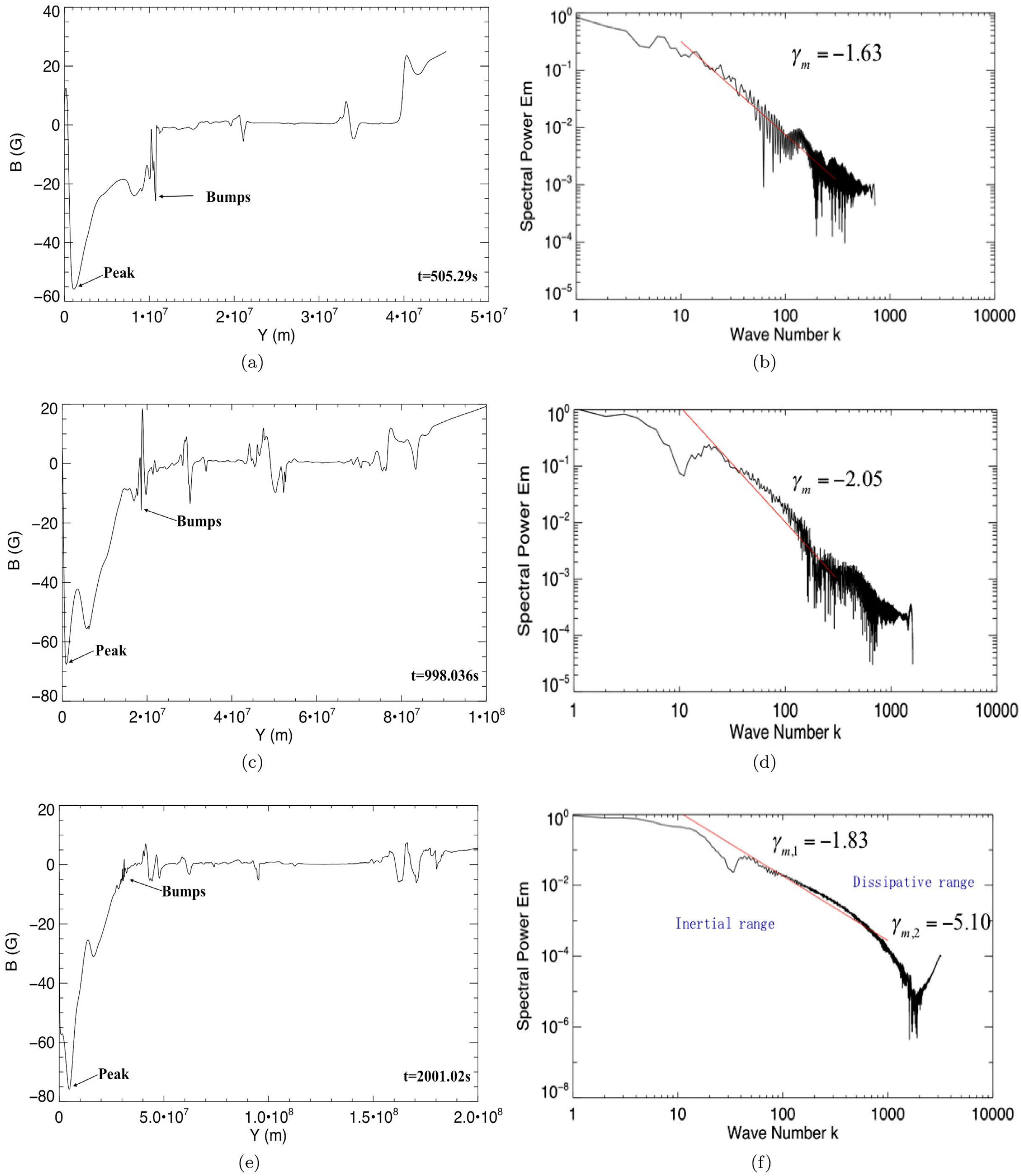

Figure 8. Distributions of the B_x component of magnetic field along $x = 0$ line covering the entire CS (left) and the corresponding magnetic spectrum power (right).

of AMR to visualize the data in the 40–160 Mm interval from $t = 4082$ to $t = 4540$ s, the magnetic nulls are usually not located on the vertices of the computational grid. Therefore, we use the nearest grid point instead of the real neutral point, under the assumption that there is only one critical point in each grid cell. After applying the above procedure, we are able to find an approximate way to describe the distribution of X-points and O-points in two dimensions without introducing false critical points by interpolation. Fig. 12(a) shows the kinematics of X- (blue cross) and O-points (red circle) in the CS projected on the y-axis from $t = 4082$ to $t = 4540$ s. We plot also the principal X-point of this CS pattern as a solid black line. It is interesting to notice that the PX point (black solid line) jumped between two points separated by a large plasmoid moving from $y \approx 7.5 \times 10^7$ to $y \approx 1.32 \times 10^8$ m. Because the existence of the upwards large plasmoid cuts the global current layer into two quasi-independent patterns, each of them has a unique principal X-point. The creation of an O-X-O configuration shows the plasmoid merging, while the splitting of the X-point into an X-O-X configu-

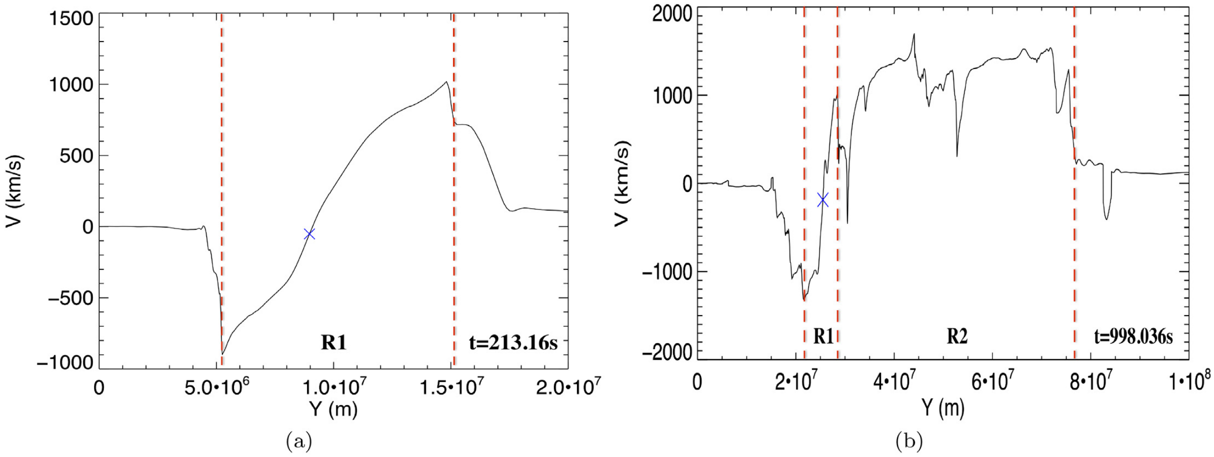

Figure 9. Distributions of the v_y component of the velocity along $x = 0$ line covering the entire CS.

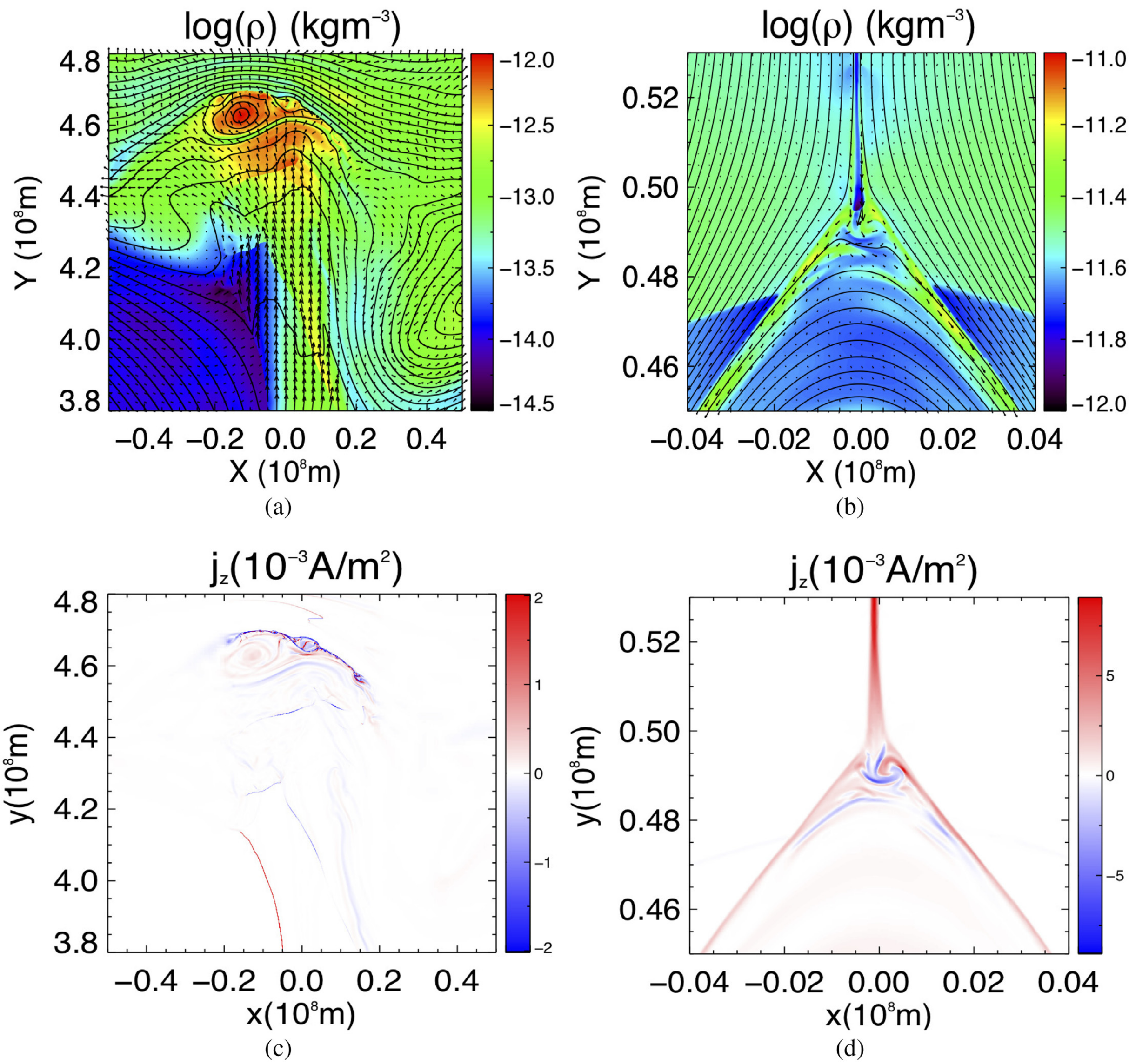

Figure 10. Snapshots at $t = 4283$ s for Run A. (a) Mass density and velocity field at the bottom of the flux rope. (b) Mass density and velocity field near the cusp structure of flare. (c) Current density at the bottom of the flux rope. (d) Current density near the cusp structure of flare.

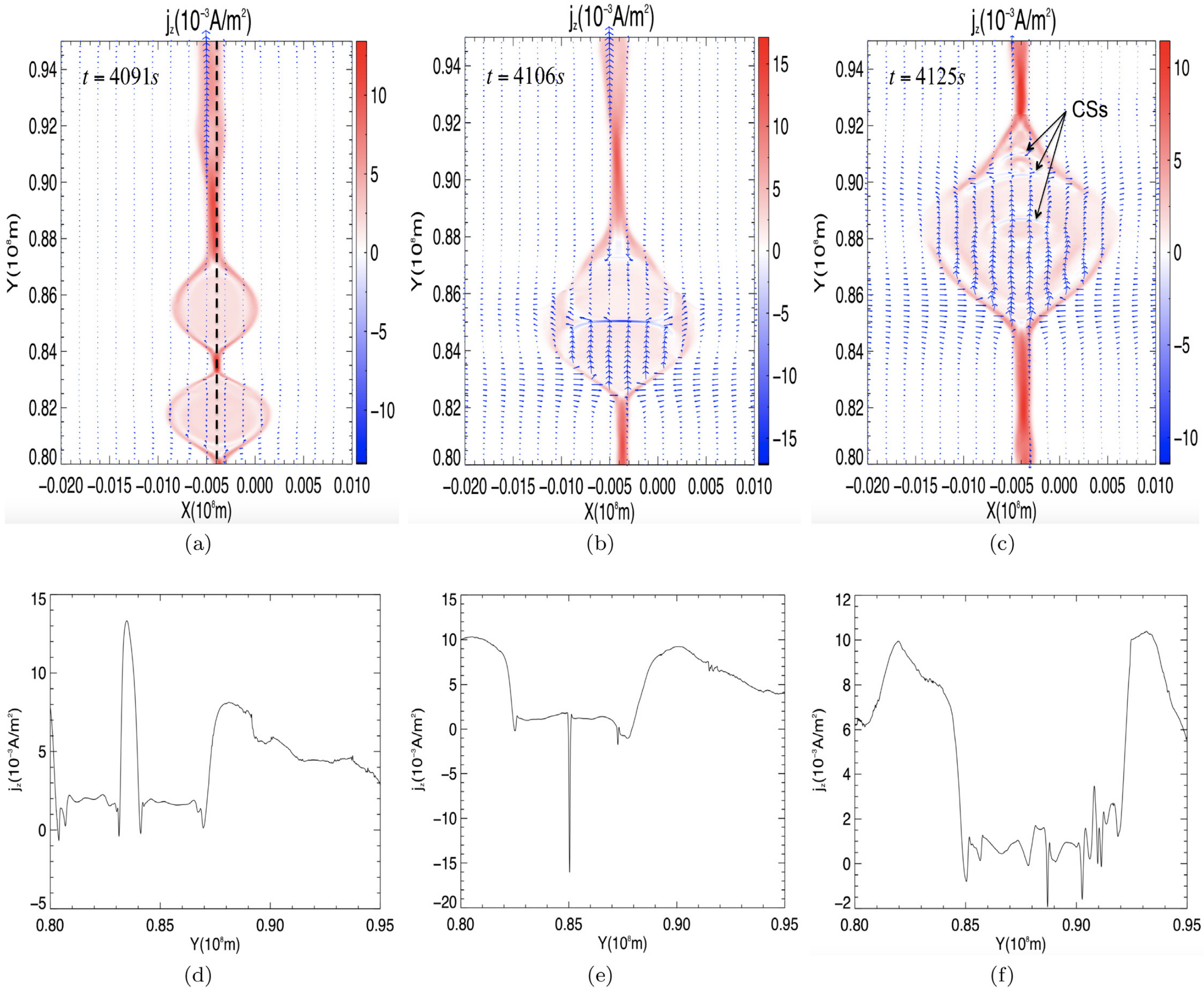

Figure 11. Current density and the velocity field, illustrating the two plasmoids coalescence for a period of 34s.

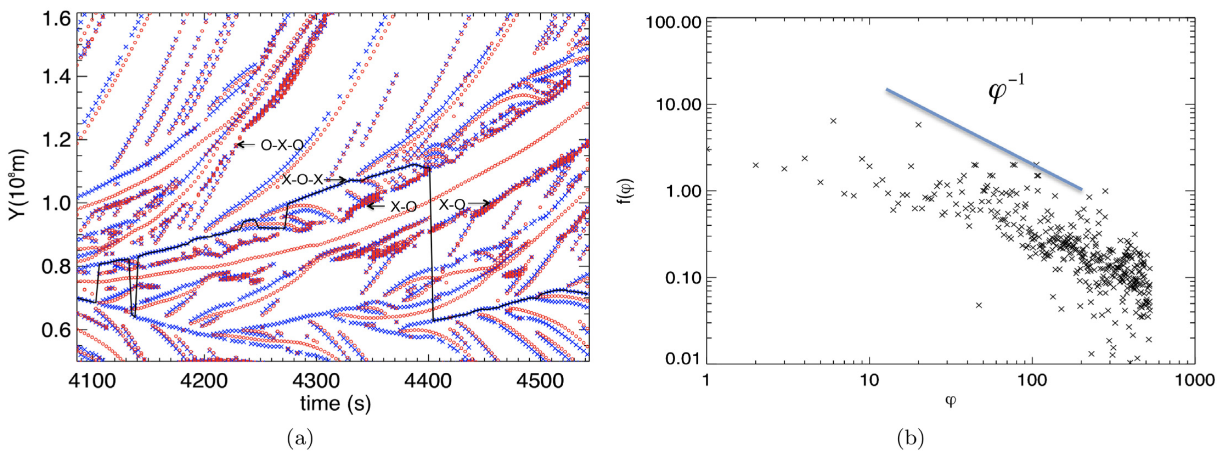

Figure 12. (a) Kinematics of magnetic nulls at t = 4082–4540 s: X-points (blue cross), O-points (red circle), and PX-point (black solid line). (b) Plasmoid flux distribution function $f(\varphi)$ versus φ.

ration maps the tearing mode instability to generate new magnetic islands (a similar scenario is depicted by fig. 3 of Fermo et al. 2011). Note also the fluctuation of temporary X-O pairs around the large plasmoid indicates the tearing in the horizontal CS formed between the coalescing plasmoids. The plasmoid flux distribution function provides a statistical understanding of the plasmoid dynamics, so it is appropriate to address that here. Using the same strategy as mentioned in Loureiro et al. (2012), Shen et al. (2011), Ni et al. (2015), we calculated the plasmoid flux distribution function defined as $f(\varphi) = -\mathrm{d}N(\varphi)/\mathrm{d}\varphi$ numerically, where $N(\varphi)$ is the number of plasmoids with magnetic flux larger than φ. Here, the magnetic flux of a magnetic island φ is measured $|\varphi_O - \varphi_X|$, with φ_O and φ_X are the magnetic potential at the O-point of the magnetic island and the magnetic potential at the nearest X-point, respectively. Fig. 12(b) gives the plasmoid flux distribution function by taking account of all the plasmoids in Fig. 12(a). Fermo, Drake & Swisdak (2010) established the rules for island merger: the merging of two islands yields an island with an area A equal to the sum of the two initial areas and a flux φ equal to the higher of the two initial fluxes. As a result, the $f(\varphi)$ in this steady cascading period behaves as a power law close to $f(\varphi) \sim \varphi^{-1}$ in the intermediate φ regime and falls off rapidly to φ^{-2} for large φ.

Following the above analysis, we are also interested in the effective reconnection properties at all filamented CSs, which provide diffusion regions to dissipate the energy at the X-points that we have identified. In particular, when a plasmoid is interacting with another plasmoid or the flare loops, we will make some effort to quantify the reconnection rates within and find out the dominant mechanism responsible for the local rates. The fact is that the local geometry of the diffusion region near each X-point is related to the Hessian eigenvalues, so we have

$$\lambda_{\max} = \frac{\partial^2 A}{\partial s^2}, \quad \lambda_{\min} = \frac{\partial^2 A}{\partial l^2}. \tag{23}$$

Note that $\lambda_{\max}$ and $\lambda_{\min}$ are larger and smaller values in magnitude, respectively. The coordinates s and l represent the minimum thickness and the elongation of the local CS. To characterize the topology of the diffusion region, we introduce the aspect ratio of the local CS in an approximative way deduced from equation (23) as follows:

$$\frac{l}{s} \simeq \sqrt{\lambda_R}, \quad \text{where} \quad \lambda_\mathrm{R} = \left|\frac{\lambda_{\max}}{\lambda_{\min}}\right|. \tag{24}$$

Following the same method of Servidio et al. (2010), a precise way to measure the local reconnection rate of CSs is to compute the electric field at the X-points. Indeed, considering the induction equation in terms of the magnetic potential $\boldsymbol{A}$, we have $-\mathrm{d}\boldsymbol{A}/\mathrm{d}t = E_z$, with $E_z = -(\boldsymbol{v} \times \boldsymbol{b})_z + \boldsymbol{j}/\sigma$ the electric field in one dimension and conductivity $\sigma = 1/(\mu\eta)$. The reconnection rate is computed as the rate of the change of the magnetic flux accumulated between the O-point and its nearby X-point:

$$\gamma(t) = \frac{\partial(\varphi_X(t) - \varphi_O(t))}{\partial t}\frac{1}{b_0 V_{A0}}, \tag{25}$$

where b_0 and V_{A0} are the magnetic field and Alfvén velocity at the centre of the initially existing flux rope. As we know, the change of the flux at the O-point remains zero, so the reconnection rate measured at each X-point is determined by

$$\gamma = E_z(\text{X-point})/b_0 V_{A0} = \mathbf{j}/\sigma b_0 V_{A0}. \tag{26}$$

Since the resistivity η in our simulations is defined to be uniform in the vicinity of the CS, the reconnection rates only vary with the current density at X-points. Fig. 13 shows the local reconnection rates of fragmented CSs as functions of their aspect ratios at different times plotted in logarithmic axes for Run A and Run B. For a case of the slow CME (Run A), the rates are plotted at $t = 1293$, 2649, 4118, 4282.83 s and vary in the range $[10^{-4}, 0.3]$. For a case of the moderate CME (Run B), the rates are plotted at $t = 393.4$, 508.3, 661.6 s and vary in the range $[10^{-3}, 0.22]$. Although the CME velocity of Run B is nearly three times larger than Run A, the rates for both runs are quite similar and do not show much dependence on the upward velocity of the flux rope. On the other hand, from the scaling analysis of equation (23), the local rates for both runs present close to a power law of 1 in terms of the geometry of diffusion regions, which is

$$\gamma \sim \lambda_R = \frac{l^2}{s^2}. \tag{27}$$

Although, the power-law fit in Fig. 13 is generally valid from slow to fast reconnection events for both CMEs, the rates saturates at $\lambda_R \sim 100$ (or $l/s \sim 10$) and remain flat afterwards. Considering the Lundquist number of our simulation tests, the global Sweet–Parker rate would be ~0.003 for Run A and ~0.002 for Run B. However, most of the reconnection rates found in our tests are much faster than expected from the Sweet–Parker model. The results for $\lambda_R < 3$ depart strongly from a power law but tend to $\sim\lambda_R$ rapidly. According to the phase-randomizing analysis by Servidio et al. (2010), we conclude that the non-linear, intermittent nature of MHD is responsible for the faster reconnection rates. Therefore, the rates from slow to fast could represent the different stages of the tearing mode developing from linear to non-linear regimes, and lastly reaching saturation.

Many analytical studies quantify the magnetic field in 3D null point topologies (Brown & Priest 2001), the current distributions near 3D null points (Rickard & Titov 1996), and solutions for fan, spine, and separator reconnection (Craig & McClymont 1999; Craig et al. 1999; Ji & Song 2001), which suggest that the magnetic reconnection in 3D is profoundly different from that in 2D (or 2.5D). As far as the discussion of the turbulent regime in 3D, the MHD simulations of Huang & Bhattacharjee (2016) reveal that 3D plasmoid instabilities in a reconnection layer can lead to a self-sustained turbulent state as well as anisotropy of eddies with respect to local magnetic field. In term of the flux rope formation, more resonant surfaces and interactions at oblique angles are possible in 3D, while 2.5D results have too much symmetry. Also, the kink instability can develop and interact with tearing mode resulting in the turbulent evolution in these 3D experiments. Although the formation and interaction of flux ropes lead to 3D turbulence, key aspects of 2D reconnection physics are surprisingly robust regarding time-scales, dissipation physics as well as particle acceleration. In particular, Guo et al. (2014, 2015, 2016) have proven, using full PIC simulations, that 3D turbulence does not significantly change the energy conversion, reconnection rate, or particle acceleration. Therefore, the consequences of our 2.5D MHD simulations regarding the energy cascading as well as turbulent reconnection can still provide a preliminary analysis of magnetic energy conversion for comparison with 3D models.

In addition, we need to point out that the CS develops in the solar eruption as a result of the severely stretching of the coronal magnetic field in a certain direction due to the loss of equilibrium in the system, and the CS is elongated roughly in this direction as well. This unfolds a scenario that the CME-flare CS indeed possesses a sheet-like feature globally with a certain amount extension in the third direction. This may help us understand why a CS is mostly observed as a straight feature, and a curved CS has never been observed, similar to the extended CS case in the solar wind at 1 au. Because of the stretching by the solar wind, an extended CS is typically highly planar and no significant warping occurs in the reconnection process (Phan, Gosling & Davis 2009). Recent 3D numerical experiments by Mei et al. (2017) displayed a manifestation of the CS that also duplicated almost every single detail that was shown in the 2D simulations by Mei et al. (2012). Furthermore, the 2017 September 10 event produced a superfast CME associated with an X-class flare, and a straight CS connecting CME to the flare just in way that both 2D analytic solution and simulation, as well

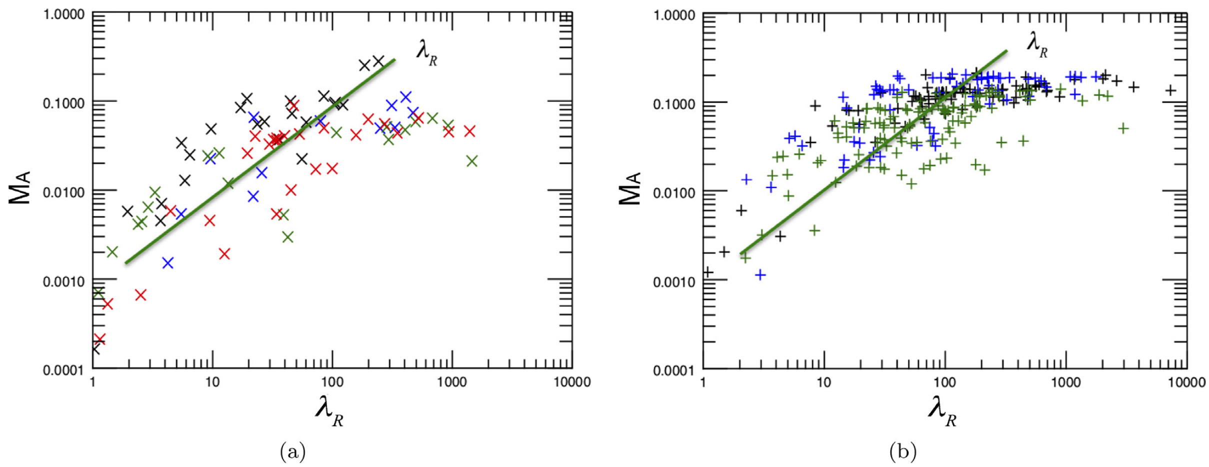

Figure 13. Local reconnection rates versus the geometry of diffusion CSs. (a) Run A for $t = 1293$ (black), 2649 (blue), 4118 (green), 4282.83 s (red). (b) Run B for $t = 393.4$ (black), 508.3 (blue), 661.6 s (green).

as 3D simulation, showed (Li et al. 2018; Seaton & Darnel 2018; Warren et al. 2018; Yan et al. 2018). However, future work of whole 3D simulations is needed to reveal cascading and fragmentation processes.

4 SUMMARY AND DISCUSSION

To study the cascading energy conversion in solar eruptions via magnetic reconnection, it is always important to understand the physical mechanisms responsible for the efficient energy dissipation and the associated fast reconnection rates. Numbers of observations (Ko et al. 2003, 2010; Webb et al. 2003; Yan et al. 2018) are consistent with the predictions of the catastrophe model (Lin & Forbes 2000), which follows the triggering and the development of typical CME events due to the loss of equilibrium. To save computing resources as well as focusing on the study of the kinetic behaviour of the flux rope, we have simulated two CMEs of different velocities using the NIRVANA code, with the eruptions starting immediately from the non-equilibrium initial state. In this work, we used the 2.5D MHD model including the resistivity, viscosity, and gravitationally stratified atmosphere. The simulation domain covers 2 solar radii above the solar surface and the empirical S&G plasma environment is adopted. In comparison with the previous work based on the Lin and Forbes model (Wang et al. 2009, 2015; Mei et al. 2012), we have a more realistic background atmosphere than the isothermal atmosphere to follow the rise of the flux rope at large altitudes (Lin 2002), a better approximation for the boundary condition set-up and a higher resolution mesh using AMR in the vicinity of the CS to capture small-scale features associated to the energy dissipation mediated by plasmoids. This provides a straightforward way to find the relationship between the overall evolution and the fine structure inside the CS responsible for fast reconnection rates. Here is the summary as follows.

(1) Two numerical experiments of CMEs of different velocities are carefully investigated, and the global dynamics features are fairly consistent with the flare model of Reeves & Forbes (2005). The estimate of the reconnection speed is related to the Alfvén speed field, and the use of S&G model yields a more reliable Alfvén speed distribution which decays at large altitudes (Lin 2002). However, the magnetic field determines the energetics of the process and the CMEs of different velocities show no difference in dynamical properties in principle. A slow CME is expected in a weak magnetic field, but if the average strength at the low base of corona is less than 27 G, the motion of the flux rope could be confined by the gravitational force resulting in an unexpected deceleration near or after 1 $R_\odot$. On the other hand, a moderate CME in a stronger magnetic field shows a continual acceleration until 1 $R_\odot$ and then propagates at nearly a constant speed afterwards.

(2) The energy is dissipated via magnetic reconnection once the CS forms. From the global view, in either the slow CME or the moderate one, more than half of the dissipated magnetic energy is converted into heating the plasma at MHD scales. The main inflow Poynting flux is devoted into the conversion of both the enthalpy flux and the kinetic energy flux of the same magnitude in the sunward direction, but the kinetic energy is dominant in the CME direction. The upper and lower termination shocks do not propagate symmetrically, nor are the associated Mach numbers symmetric.

(3) The fragmentation of the global current layer consists of both tearing and coalescence processes, which form multiple CSs to facilitate the magnetic energy dissipation. The CSs are filamented down to the finest resolution due to the formation of plasmoids, and the filamented CSs of coalescence are perpendicular to the tearing ones as well as have the opposite current polarity. Moreover, the typical lifetime of a plasmoid merging process could last over 0.5 per cent of the total simulation time, and these events occur frequently when plasmoids interact with the flare loops at the bottom of the flux rope and collide with other plasmoids inside the global current layer. Therefore, the cascading reconnection definitely has an important effect on the intermittency of the total reconnection speed.

(4) The energy cascade ends at ≈200 km according to a 1D Fourier spectrum analysis for magnetic energy, which is consistent with the smallest recognizable CSs in these simulations. The magnetic energy spectral index varies in the range [1.6, 2.1] for the whole calculation. In the early stages, the spectrum follows a single power law of index 1.6. When magnetic islands keep on growing, the spectral distribution starts to change from the single power law, but the largest dominant index is 2.1. After the appearance of secondary islands, the dominant spectrum index flattens. Investigating the balance between the tearing and the cascading processes, we have the index of 1.83 for the inertial range as well as that of 5.1 for the dissipative range. The shape of the spectrum does not fol-

low a single power law anymore, and the dissipation takes place at macroscales much greater than kinetic scales.

(5) We track also the kinematics of the magnetic nulls for a period of time to study the crucial reason for the local reconnection rates. We observe various configurations that signify the different behaviours of plasmoids. The corresponding plasmoid distribution function behaves as a power law close to φ^{-1} in the intermediate φ phase. However, the local reconnection rates for both runs vary in the same range $[10^{-4}, 0.3]$ irrespective of the kind of CME (slow or moderate), but they present a relationship to the local topology of CSs which are closely proportional to the square of the aspect ratios. No matter how strong the magnetic field or how long the global current layer is, the local geometry of the filamented CSs seems to be similar. The corresponding local rates follow a scaling law $\sim\lambda_R$, and eventually saturate under 0.3 for both cases.

Overall, the dynamic evolution and physical properties of the model CME/flare CS in our simulations are greatly in agreement with observational results for typical large-scale CSs. These features include high-speed upward and downward outflows, slow condensation inflows, large-scale dense plasma blobs inside the CS (see Lin et al. 2015 for more details). Although the energy released in our simulations is several orders smaller than the observational estimate in Emslie et al. (2005), the asymmetrical energy partition in solar eruptions is consistent with Reeves et al. (2010). Also, recognizable blobs in the wake of CME were found in LASCO C2 and C3, and the change in the velocity of those blobs suggests a non-uniform structure of the CS (Lin et al. 2005). Turbulent features inside the post-CME CS reported by Li et al. (2018) can be explained by the cascading process in this work, which could be important for rapid reconnection. However, since no cooling mechanism is included here, the simulated temperature is an upper limit to that in reality and we cannot calculate the flare emissions to compare directly with observations. Taking advantage of the simplicity and symmetry of a 2.5D simulation, we plan to analyse the thermal structure of the CME/flare CS as well as the plasma heating via turbulence by including thermal conduction and optical thin radiative cooling in the future.

ACKNOWLEDGEMENTS

JY is grateful to N. A. Murphy, Z. X. Mei, and Q. W. Cai for valuable discussions. The authors would like to thank the editor and the anonymous referee for the valuable and constructive comments and suggestions that helped improve this work significantly. This work was supported by the Strategic Priority Research Programme of Chinese Academy of Sciences (CAS) with grants XDA17040507, XDA15010900, and QYZDJ-SSWSLH012, Programme 973 grant 2013CBA01503, National Natural Science Foundation of China (NSFC) grants 11603070, 11333007, U1631130, and the grant associated with the project of the Group for Innovation of Yunnan Province, as well as the Special Programme for Applied Research on Super Computation of the NSFC-Guangdong Joint Fund (nsfc2015_461). CS acknowledges the support by National Science Foundation of U.S. grants AGS-1358342, AGS-1723313, AGS-1723425 to the Smithsonian Astrophysical Observatory. JCR and CS were supported by the NASA LWS programme through ROSES NNH13ZDA001N.

REFERENCES

Amari T., Luciani J. F., Aly J. J., Mikic Z., Linker J., 2003, ApJ, 585, 1073
Antiochos S. K., DeVore C. R., Klimchuk K. A., 1999, ApJ, 510, 485
Bemporad A., Poletto G., Suess S. T., Ko Y.-K., 2006, ApJ, 638, 1110
Brown D. S., Priest E. R., 2001, A&A, 367, 339
Bárta M., Büchner J., Karlický M., Skála J., 2011, ApJ, 737, 24
Chen B., Bastian T. S., Shen C., Gary D. E., Krucker S., Glesener L., 2015, Science, 350, 1238
Chen P. F., Shibata K., 2000, ApJ, 545, 524
Ciaravella A., Raymond J. C., 2008, ApJ, 686, 1372
Ciaravella A., Raymond J. C., Li J., Reiser P., 2002, ApJ, 575, 1116
Cowling T. G., 1953, The Sun. University of Chicago Press, Chicago
Craig I. J. D., Fabling R. B., Heerikhuisen J., Watson P. G., 1999, ApJ, 523, 838
Craig I. J. D., McClymont A. N., 1999, ApJ, 510, 1045
Ding Y. J., Hong Q. F., Wang H. Z., 1987, Sol. Phys., 107, 221
Emslie A. G., Dennis B. R., Holman G. D., Hudson H. S., 2005, J. Geophys. Res., 110, A11103
Fermo R. L., Drake J. F., Swisdak M., 2010, Phys. Plasmas, 17, 010702
Fermo R. L., Drake J. F., Swisdak M., Hwang K.-J., 2011, J. Geophys. Res., 116, A09226
Feynman J., Martin S. F., 1995, J. Geophys. Res., 100, 3355
Forbes T. G., 1990, J. Geophys. Res., 95, 11919
Forbes T. G., 1991, Geophys. Astrophys. Fluid Dyn., 62, 15
Forbes T. G., 2000, J. Geophys. Res., 105, 23153
Forbes T. G., Priest E. R., 1984, Sol. Phys., 94, 315
Forbes T. G., Priest E. R., Isenberg P. A., 1994, Sol. Phys., 150, 245
Forbes T. G., Seaton D. B., Reeves K. K., 2018, ApJ, 858, 70
Forbes T. G. et al., 2006, CME Theory and Models. In: Coronal Mass Ejections. Space Sciences Series of ISSI. Springer-Verlag, New York
Furth H. P., Killeen J., Rosenbluth M. N., 1963, Phys. Fluids, 6, 459
Guo F., Li H., Daughton W., Liu Y.-H., 2014, Phys. Rev. Lett., 113, 155005
Guo F., Li H., Daughton W., Li X., Liu Y.-H., 2016, Phys. Plasmas, 23, 055708
Guo F., Liu Y.-H., Daughton W., Li H., 2015, ApJ, 806, 167
Huang Y.-M., Bhattacharjee A., 2016, ApJ, 818, 20
Innes D. E., McKenzie D. E., Wang T., 2003, Sol. Phys., 217, 247
Isenberg P. A., Forbes T. G., Demoulin P., 1993, ApJ, 417, 368
Jelínek P., Karlický M., Van Doorsselaere T., Bárta M., 2017, ApJ, 847, 98
Jiang C., Feng X., Wu S. T., Hu Q., 2012, ApJ, 759, 85
Ji H. S., Song M. T., 2001, ApJ, 556, 1017
Karpen J., S.K. A., DeVore C., 2012, ApJ, 760, 46
Kopp R. A., Pneuman G. W., 1976, Sol. Phys., 50, 85
Ko Y.-K., Raymond J. C., Lin J., Lawrence G., Li J., Fludra A., 2003, ApJ, 594, 1068
Ko Y.-K., Raymond J. C., Vrsnak B., Vujić E., 2010, ApJ, 722, 625
Lazarian A., Vishniac E. T., 1999, ApJ, 517, 700
Lin J., 2002, Chin. J. Astron. Astrophys., 2, 539
Lin J., Forbes T. G., 2000, J. Geophys. Res., 105, 2375
Lin J., Ko Y.-K., Sui L., Raymond J. C., Stenborg G. A., Jiang Y., Zhao S., Mancuso S., 2005, ApJ, 622, 1251
Lin J., Murphy N. A., Shen C., Raymond J. C., Reeves K. K., Zhong J., Wu N., Li Y., 2015, Space Sci. Rev., 194, 237
Linsky J. L., Avrett E. H., 1970, PASP, 82, 485
Liu R., Lee J., Wang T., Stenborg G., Liu C., Wang H., 2010, ApJ, 723, L28
Li Y. et al., 2018, ApJ, 853, L15
Loureiro N. F., Samtaney R., Schekochihin A. A., Uzdensky D. A., 2012, Phys. Plasmas, 19, 042303
Loureiro N. F., Schekochihin A. A., Cowley S. C., 2007, Phys. Plasmas, 14, 100703
Lynch B. J., Gruesbeck J. R., Zurbuchen T. H., Antiochos S. K., 2005, J. Geophys. Res., 110, A08107
Mackay D. H., van Ballegooijen A. A., 2009, Sol. Phys., 260, 321
Mei Z., Lin J., 2008, New Astron., 13, 526
Mei Z., Shen C., Wu N., Lin J., Murphy N. A., Roussev I. I., 2012, MNRAS, 425, 2824
Mei Z. X., Keppens R., Roussev I. I., Lin J., 2017, A&A, 604, L7

Mikić Z., Linker J. A., 1994, ApJ, 430, 898
Ni L., Kliem B. H., Lin J., Wu N., 2015, ApJ, 799, 79
Ni L., Lin J., Murphy N. A., 2013, Phys. Plasmas, 20, 061206
Ni L., Roussev I. I., Lin J., Ziegler U., 2012b, ApJ, 758, 20
Ni L., Ziegler U., Lin J., Mei Z., 2012a, Phys. Plasmas, 19, 072902
Nishida K., Nishizuka N., Shibata K., 2013, ApJ, 775, L39
Orlanski I., 1976, Comput. Phys., 21, 251
Patsourakos S., Vourlidas A., 2010, A&A, 525, 27
Petschek H. E., 1964, NASA Special Publication, 50, 425
Phan T. D., Gosling J. T., Davis M. S., 2009, Geophys. Res. Lett., 36, L09108
Priest E. R., Forbes T. G., 2000, Magnetic Reconnection: MHD Theory and Applications. Cambridge Univ. Press, Cambridge
Rana S., 2004, Surface Topological Data Structures: An Introduction for Geo- graphical Information Science. Wiley, Chichester
Raymond J. C., Ciaravella A., Dobrzycka D., Strachan L., 2003, ApJ, 597, 1106
Reeves K. K., Forbes T. G., 2005, ApJ, 630, 1133
Reeves K. K., Golub L., 2011, ApJ, 727, L52
Reeves K. K., Linker J. A., Mikić Z., Forbes T. G., 2010, ApJ, 721, 1547
Rickard G. J., Titov V. S., 1996, ApJ, 472, 840
Savage S. L., Holman G., Reeves K. K., Seaton D. B., McKenzie D. E., Su Y., 2012, ApJ, 754, 13
Schmieder B., Démoulin P., Aulanier G., 2013, Adv. Space Res., 51, 1967
Seaton D. B., Darnel J. M., 2018, ApJ, 852, L9
Servidio S., Matthaeus W. H., Shay M. A., Dmitruk P., Cassak P. A., Wan M., 2010, Phys. Plasmas, 17, 032315
Shen C., Lin J., Murphy N. A., 2011, ApJ, 737, 14
Shen C., Lin J., Murphy N. A., Raymond J. C., 2013, Phys. Plasmas, 20, 072114
Sittler E. C., Guhathakurta M., 1999, ApJ, 523, 812
Song H. Q., Chen Y., Qiu J., Chen C. X., Zhang J., Chen X., Shen Y. D., Zheng R. S., 2018, ApJ, 857, L21
St. Cyr O. C., Plunkett S. P., Michels D. J., 2000, J. Geophys. Res., 1005, 18169
Svestka Z., 2001, Space Sci. Rev., 95, 135
Takahashi T., Qiu J., Shibata K., 2017, ApJ, 848, 102
Titov V., Démoulin B., 1999, A&A, 351, 707
Török T., Kliem B., 2005, ApJ, 630, L97
Wang H., Liu S., Gong J., Wu N., Lin J., 2015, ApJ, 805, 114
Wang H., Shen C., Lin J., 2009, ApJ, 700, 1716
Warren H. P., Brooks D. H., Ugarte-Urra I., Reep J. W., Crump N. A., Doschek G. A., 2018, ApJ, 854, 122
Webb D. F., Burkepile J., Forbes T. G., 2003, J. Geophys. Res., 108, 1440
Xie X. Y., Ziegler U., Mei Z. X., Wu N., Lin J., 2017, Acta Astron. Sin., 58, 004
Yan X. L., Huang L. H., Xue Z. K., Mei Z. X., Kong D. F., Wang J. C., Li Q. L., 2018, ApJ, 853, L18
Yan X. L., Qu Z. Q., Kong D. F., Xu C. L., 2012, ApJ, 754, 16
Ziegler U., 2004, J. Comput. Phys., 196, 393
Ziegler U., 2005, Comput. Phys. Commun., 170, 153
Ziegler U., 2008, Comput. Phys. Commun., 179, 227
Ziegler U., 2011, J. Comput. Phys., 230, 1035

This paper has been typeset from a TEX/LATEX file prepared by the author.